

**Comparison of low refrigerant charge, air-coupled and hydronically coupled
microchannel heat pumps with conventional systems**

by

Yirong Jiang

A thesis submitted to the graduate faculty
in partial fulfillment of the requirements for the degree of
MASTER OF SCIENCE

Major: Mechanical Engineering
Major Professor: Srinivas Garimella

Iowa State University

Ames, Iowa

2001

Copyright © Yirong Jiang 2001. All rights reserved

Graduate College
Iowa State University

This is to certify that the Master's thesis of
Yirong Jiang
has met the thesis requirements of Iowa State University

Signatures have been redacted for privacy

*To my husband—Yongjun Hou
For his love and support.*

TABLE OF CONTENTS

LIST OF FIGURES	vi
LIST OF TABLES	ix
ACKNOWLEDGEMENTS	x
ABSTRACT	xi
CHAPTER 1. INTROUDUCTION AND BACKGROUND	1
State of the Art	1
Air-coupled system	1
Hydronically coupled system	5
Research Objectives and Approach	7
CHAPTER 2. OVERALL SYSTEM MODELING	8
Conventional Round-Tube/Flat Fin System	8
Microchannel Heat Pump Systems	10
Air-Coupled System	11
Results from the ideal air-coupled heat pump model	16
Hydronically coupled system	18
Results from the ideal hydronically coupled heat pump model	22
CHAPTER 3. HEAT EXCHANGER MODELING	26
Overview of Heat Exchanger Modeling Procedures	26
Geometry calculation	30
Tube side	30
Air side	31
Heat transfer and pressure drop calculation	34
Single-phase heat transfer and pressure drop	34
Two-phase heat transfer coefficient and pressure drop	35
Air-side heat transfer and pressure drop	38
Overall heat transfer calculation for dry surface air-coupled heat exchanger	39
Overall heat transfer calculation for wet surface air-coupled heat exchanger	40
Overall heat transfer calculation for hydronically coupled heat exchanger	41
Results for the Component Designs Using Lumped Heat Exchanger Model	41
CHAPTER 4. COMPRESSOR MODELING	45
CHAPTER 5. INCREMENTAL ANALYSIS OF TWO-PHASE HEAT TRANSFER	50
CHAPTER 6. COMPARISONS OF THE TWO SYSTEMS	69

CHAPTER 7. CONCLUSIONS	78
BIBLIOGRAPHY	80

LIST OF FIGURES

Figure 1.	Schematic of Air Coupled System	2
Figure 2.	Round Tube Heat Exchanger Geometry with Different Fins	3
Figure 3.	Geometry of Microchannel Air-Coupled Heat Exchanger	4
Figure 4	Microchannel Tube and Louvered Fin details	4
Figure 5.	Schematic of a Hydronically Coupled System (Cooling Mode)	5
Figure 6.	Configuration of a Microchannel Refrigerant-to-Hydraulic Fluid Heat Exchanger	6
Figure 7.	Air-Coupled System P-h Diagram	12
Figure 8.	Air-Coupled System Modeling Procedure	14
Figure 9.	The Effect of CAT on System COP (Heating Mode)	15
Figure 10.	The Effect of CAT on Heat Exchanger UAs (Heating Mode)	16
Figure 11.	Effect of Ambient Temperature on Heating Mode COP	19
Figure 12.	Effect of Ambient Temperature on Heating Mode Performance (Air-Coupled System)	19
Figure 13.	Effect of Ambient Temperature on Cooling Mode COP (Air-Coupled System)	20
Figure 14.	Effect of Ambient Temperature on Cooling Mode Performance (Air-Coupled System)	20
Figure 15.	Hydronically Coupled System P-h Diagram (Air-Coupled System)	21
Figure 16.	Effect of Ambient Temperature on Cooling Mode Performance (Hydronically Coupled System)	25
Figure 17.	Effect of Ambient Temperature on Heating Mode Performance (Hydronically Coupled System)	25
Figure 18.	Geometric Details of A Microchannel Tube	30
Figure 19.	Geometric Details of A Multilouver Fin	32
Figure 20	Fin-Side Heat Transfer Area	33
Figure 21	Energy Balance for the Compressor (Fischer and Rice, 1983)	46
Figure 22.	Compressor Modeling Procedure	48
Figure 23.	Temperature Profile in the Air-Coupled Condenser	52
Figure 24.	Required UA Per Segment in the Air-Coupled Condenser	52
Figure 25.	Heat Transfer Resistances in the Air-Coupled Condenser	53

Figure 26.	Length Required Per Quality Increment in the Air-Coupled Condenser	53
Figure 27.	Refrigerant Pressure Drop Variation with Average Quality (Air-Coupled Condenser)	54
Figure 28.	Air-Side Pressure Drop Variation Across the Air-Coupled Condenser	54
Figure 29.	Temperature Profile in the Air-Coupled Evaporator	55
Figure 30.	Thermal Conductivity of Water Film on the Fins	56
Figure 31.	Coefficient $b_{m,w}$ as a Function of Refrigerant Average Quality	57
Figure 32.	Convective Heat Transfer Coefficient between Air and Water Film Surface	57
Figure 33.	Heat Transfer Coefficient Variation in the Air-Coupled Evaporator	58
Figure 34.	Required UA in Air-Coupled Evaporator	59
Figure 35.	Length Required Per Quality Increment in Air-Coupled Evaporator	59
Figure 36.	Critical Refrigerant Quality as a Function of Tube Diameter	60
Figure 37.	Refrigerant Pressure Drop Variation in the Air-Coupled Evaporator	61
Figure 38.	Air Side Wet-Surface Pressure Drop in the Air-Coupled Evaporator	61
Figure 39.	Temperature Profile in the Hydronically Coupled Condenser	62
Figure 40.	Required Heat Exchanger UA in Hydronically Coupled Condenser	63
Figure 41.	Heat Transfer Resistances in the Hydronically Coupled Condenser	63
Figure 42.	Length Required Per Quality Increment in the Hydronically Coupled Condenser	64
Figure 43.	Refrigerant Pressure Drop Per Quality Increment (Hydronically Coupled Condenser)	64
Figure 44.	Hydronic Fluid Pressure Drop Per Quality Increment (Hydronically Coupled Condenser)	65
Figure 45.	Temperature Profile in Hydronically Coupled Evaporator	66
Figure 46.	Required Heat Exchanger UA Per Quality Increment (Hydronically Coupled Evaporator)	66
Figure 47.	Heat Transfer Resistance Variation with Average Quality (Hydronically Coupled Evaporator)	67
Figure 48.	Length Required As a Function of Average Quality (Hydronically Coupled Evaporator)	67
Figure 49.	Critical Refrigerant Quality for Dryout as a Function of Tube Diameter	68

Figure 50.	Refrigerant Pressure Drop Per Quality Increment (Hydronically Coupled Evaporator)	69
Figure 51.	Hydronic Fluid Pressure Drop Per Quality Increment (Hydronically Coupled Evaporator)	69
Figure 52.	Variation of the Round-Tube Heat Pump Cooling Mode COP with Indoor Unit Tube and Fin Geometry	71
Figure 53.	Variation of the Round-Tube Heat Pump Cooling Mode COP with Indoor Unit Design Parameters: Overall Dimensions, Circuiting and Air Flow	71
Figure 54.	Variation of the Round-Tube Heat Pump Cooling Mode COP with Outdoor Unit Tube and Fin Geometry	73
Figure 55.	Variation of the Round-Tube Heat Pump Cooling Mode COP with Outdoor Unit Design Parameters: Overall Dimensions, Circuiting and Air Flow	73
Figure 56.	Heat Exchanger Face Area Comparison	77
Figure 57.	Overall Comparison of the Three Systems	78

LIST OF TABLES

Table 1.	Nominal Design Conditions	8
Table 2.	State Points in Air-Coupled System	12
Table 3.	State Points of Air-Coupled System Designed for Cooling Mode	17
Table 4.	Performance of Air-Coupled System Designed for Cooling Mode	17
Table 5.	State Points of Air-Coupled System Designed for Heating Mode	18
Table 6.	Performance of Air-Coupled System Designed for Heating Mode	18
Table 7.	State Points of Hydronically Coupled System Designed for Cooling Mode	23
Table 8.	Performance of Hydronically Coupled System Designed for Cooling Mode	23
Table 9.	State Points of Hydronically Coupled System Designed for Heating Mode	24
Table 10.	Performance of Hydronically Coupled System Designed for Heating Mode	24
Table 11.	Heat Exchangers Modeled in This Study	26
Table 12.	Input Geometry Features and Properties for Air-Coupled Heat Exchangers	27
Table 13.	Input Geometry Features and Properties for Hydronically Coupled Heat Exchangers	27
Table 14.	Design Conditions for Air-Coupled Heat Exchangers	28
Table 15.	Design Conditions for Hydronically Coupled Heat Exchangers	29
Table 16.	Optimized Heat Exchanger Sizes	43
Table 17.	Geometric Features of the Optimized Air-Coupled Heat Exchangers	43
Table 18.	Geometric Features of the Optimized Hydronically Coupled Heat Exchangers	43
Table 19.	State Points of Air-Coupled System Designed for Heating Mode	44
Table 20.	Performance of Air-Coupled System Designed for Heating Mode	44
Table 21.	State Points of Hydronically Coupled System Designed for Heating Mode	44
Table 22.	Performance of Hydronically Coupled System Designed for Heating Mode	45
Table 23.	Input Variables for the Compressor Model	47
Table 24.	Baseline Configuration of the Round-Tube Heat Pump	70
Table 25.	Characteristics of the Baseline Round-Tube Heat Pump	70
Table 26.	Material Volumes of the Heat Exchangers	75
Table 27.	Refrigerant Volume	75

Table 28	Dimensions of Refrigerant Lines	76
Table 29	Refrigerant Charge	76

ACKNOWLEDGEMENTS

I would like to take this opportunity to express my sincerest and deepest gratitude to my major professor, Dr. Srinivas Garimella, for his commitment to education and willingness to lend his guidance and support to me throughout the course of this study. I would also like to thank my committee members—Drs. Ron Nelson and Surya Mallapragada, for their considerate guidance and constructive suggestions to this study. Special thanks to Drs. Gregory Maxwell and Michael Pate, their input and direction were invaluable.

I also extend my thanks to my parents, Huiling Ni and Zhengxing Jiang. They provided me with “roots to grow” and “wings to fly.” Throughout my whole lifetime, they have provided opportunities and urged me to do my best.

Last but not the least, my heartfelt appreciation goes to my beloved husband, Yongjun Hou, who made it possible to begin and to complete this journey. Without him, my life would have been totally different.

ABSTRACT

Air-conditioning systems are significant contributors to the global climate change problem. Refrigerant leaks during operation, maintenance, and improper disposal at the end of their useful life contribute to the ozone-depletion and global warming problem. In addition, systems with low efficiencies indirectly contribute to the problem through fossil fuel derived greenhouse gas emissions at the power plant.

In the present study, two novel concepts for residential and commercial heat pumps using microchannel evaporator and condenser were investigated: air-coupled and hydronically coupled systems. The thermodynamic simulation models for both air-coupled and hydronically coupled heat pumps in the cooling and heating modes were designed using Engineering Equation Solver software. Performance mapping as a function of ambient conditions and component design were conducted. Heat loads, refrigerant-to-glycol and glycol-to-air temperature differences, and system COPs over the entire heating and cooling season were calculated using this model. Information on component state points were then used along with the appropriate flow mechanism-based heat transfer and pressure drop correlations to compute the configuration and size of each component that would meet these requirements. The components were optimized based on capital and operating costs to develop a system with the lowest life-cycle costs.

Results show that the microchannel heat pump would provide heating and cooling in a package much smaller than conventional systems. Both air-coupled and hydronically coupled systems also result in significant reductions in refrigerant inventories compared to the round tube systems investigated in the present study.

This concept is a new approach toward the design, fabrication and installation of heating and cooling equipment. The resulting technology is compact, modular, thermally efficient, and easy to fabricate and install. The drastic reductions in size yield substantial first-cost savings. The lower refrigerant inventories will minimize CFC and HCFC releases to the atmosphere, thus alleviating the ozone-depletion and global warming problems.

CHAPTER 1. INTRODUCTION AND BACKGROUND

Vapor compression systems are commonly used for space-conditioning applications in the world today. Most residential heat pumps are air-coupled, with four basic components: compressor, evaporator, condenser and expansion device. A large majority of these heat pumps use round-tube/flat-fin heat exchangers. However, the relatively low heat transfer coefficient on the tube-side and air-side of round-tube/flat-fin heat exchangers would typically result in large heat exchangers and refrigerant inventories.

CFC and HCFC-based refrigerants are being phased out because of their contribution to the ozone depletion and global warming problems (ASHRAE, 1997). Due to their great stability, CFCs could persist in the atmosphere for many years and eventually diffuse into the stratosphere. Once CFC-based refrigerants reach the upper atmosphere, their molecules break down and release chlorine, which could destroy the ozone layer. At lower regions of the atmosphere, these molecules absorb infrared radiation, which may contribute to global warming. However, R22 has been widely used and still being used in residential vapor compression systems. As ozone depletion and global warming become more and more of a concern, large systems with a large refrigerant charge may have a higher potential to be hazardous to the environment. A direct method to decrease the contribution from air conditioning systems to these environmental problems is to reduce the refrigerant inventories; a more indirect method to reduce global warming is to develop systems with high efficiencies. Highly efficient systems would require less electrical energy and thus indirectly reduce the contribution to global warming by reducing fossil fuel derived greenhouse gas emissions.

State of the Art

Two types of systems could be considered for residential heat pump applications: air-coupled systems and hydronically coupled systems.

Air coupled system

Air-coupled systems are widely used in residential heat pumps. Figure 1 shows the schematic of an air-coupled system. As shown in the figure, these systems are simple and

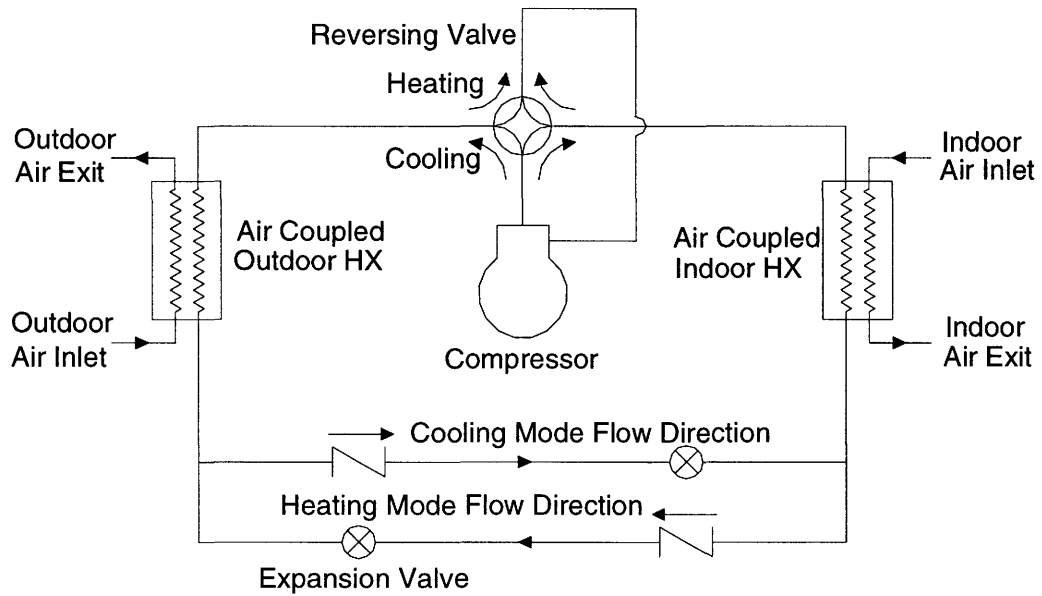


Figure 1. Schematic of Air Coupled System

have few components. The refrigerant is coupled directly to the conditioned air and outdoor ambient in such systems.

The round-tube/plate-fin geometry has been used to design air-coupled heat exchangers in space-conditioning systems for decades. These heat exchangers are used for a variety of applications ranging from large commercial refrigeration systems to small residential air conditioners. Much literature is available on heat and mass transfer in round-tube/plate-fin heat exchangers. Figure 2 shows examples of round tube heat exchangers with several different types of fins. However, the air-side heat transfer coefficient in air-coupled systems is inherently low, resulting in large heat exchangers. In addition, a refrigerant reversing valve needs to be used in such systems to switch from the cooling mode to the heating mode. The indoor and outdoor heat exchangers function as evaporator and condenser in the cooling mode, respectively, while in the heating mode, they function as condenser and evaporator, respectively. This means that in both cooling and heating modes, neither heat exchanger operates at its optimal conditions.

Highly compact, microchannel tube/multilouver fin heat exchangers have replaced the

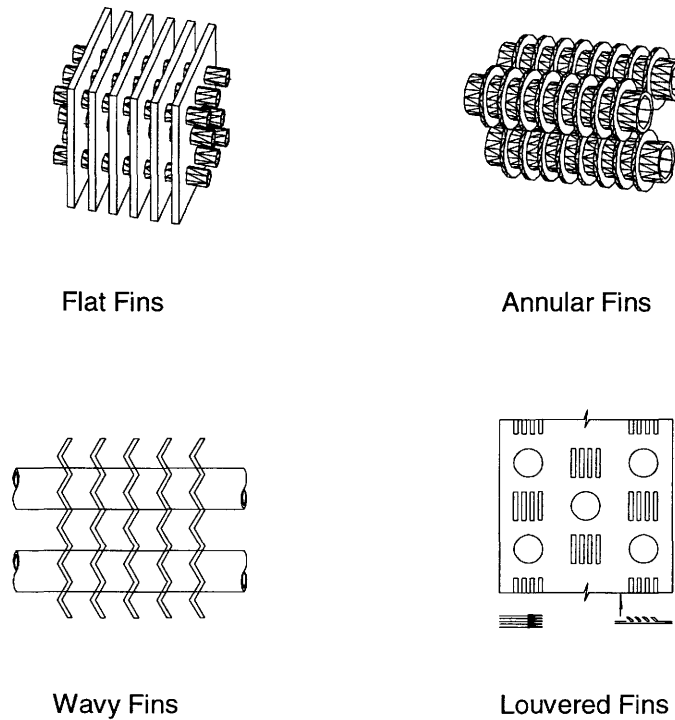


Figure 2. Round Tube Heat Exchanger Geometry with Different Fins

conventional round-tube/plate-fin geometry in automotive engine cooling and air conditioning systems. Studies (Garimella *et al.*, 1995, 1996) have shown that heat transfer coefficients for the multilouver fins are considerably higher than those for the conventional fins. This is because the interrupted fins initiate a new boundary layer with the associated high heat transfer coefficient at each louver. Furthermore, the tube-side heat transfer coefficient in microchannel tubes is much higher than the corresponding heat transfer coefficient in conventional round tubes. This is because the heat transfer coefficient is inversely proportional to tube diameter. The relatively high heat transfer coefficients on both sides lead to compact geometries. Figure 3 and Figure 4 show schematics of air-coupled microchannel heat exchangers.

The advantages of air-coupled microchannel heat exchangers also include smaller frontal obstruction to the air flow compared to round tubes, and larger surface area per unit

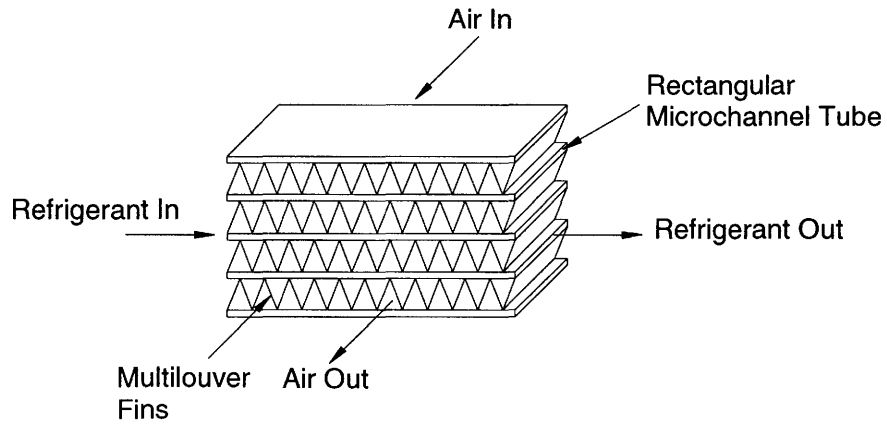


Figure 3. Geometry of Microchannel Air-Coupled Heat Exchanger

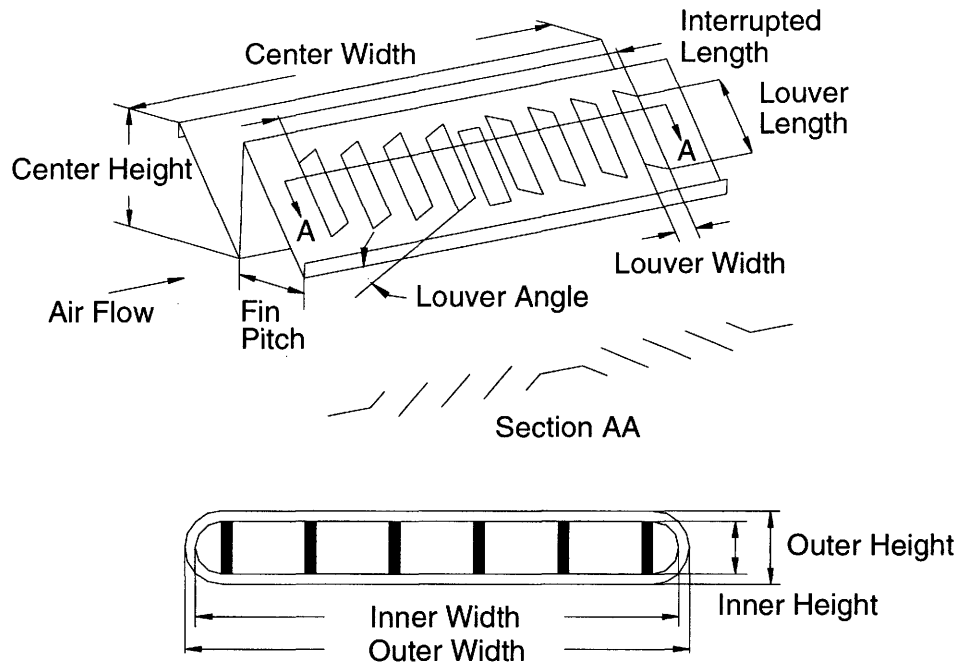


Figure 4. Microchannel Tube and Louvered Fin Details

volume. Smaller frontal obstruction reduces the drag and fan power; and large surface area/volume ratio results in compactness. Compact geometries would, in turn, result in low refrigerant inventories. These advantages could also benefit residential space-conditioning systems. Microchannel heat exchangers also offer design flexibility through the optimization of tube size, shape, number of channels, fin parameters and pass arrangement.

Hydronically coupled system

In a hydronically coupled system, the cooling/heating duty is transferred first to a hydronic fluid and then to air through the use of air-to-hydronic fluid heat exchangers. Thus, the hydronically coupled system needs two more heat exchangers compared to an air-coupled system. A hydronically coupled system therefore includes a compressor, expansion device, hydronic fluid-to-refrigerant condenser, hydronic fluid-to-refrigerant evaporator, and two air-to-hydronic fluid heat exchangers on the hot and cold sides. Figure 5 shows a schematic of a hydronically coupled system. A schematic of a hydronically coupled heat exchanger is shown in Figure 6.

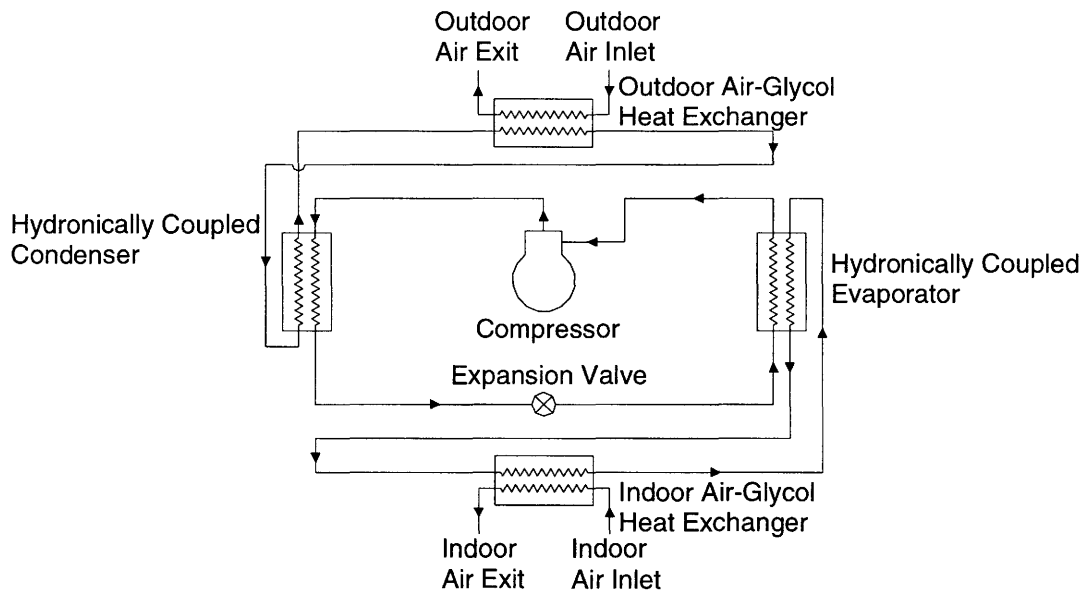


Figure 5. Schematic of a Hydronically Coupled System (Cooling Mode)

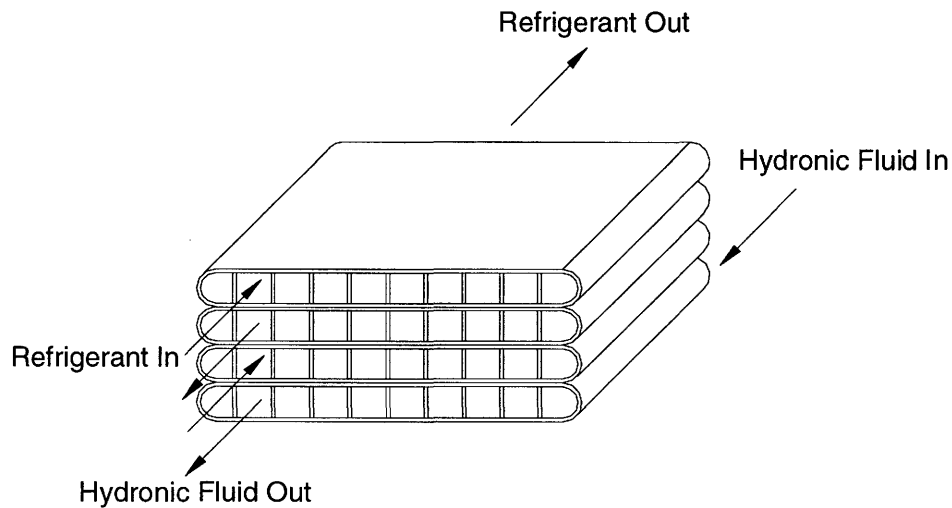


Figure 6. Configuration of a Microchannel Refrigerant-to-Hydronic Fluid Heat Exchanger

The indirect heat exchange in a hydronically coupled system introduces additional temperature difference requirements between the refrigerant and indoor and outdoor air. Ordinarily, these additional temperature differences would reduce the coefficient of performance of the system. However, the extremely high heat transfer coefficients on both the refrigerant and hydronic fluid sides of a microchannel heat exchanger would minimize this penalty while maintaining acceptable heat exchanger sizes. In fact, the high heat transfer coefficients on both sides, coupled with the pure counterflow arrangement, would result in extremely small refrigerant-hydronic fluid heat exchangers. In addition, hydronic coupling implies that the evaporator and condenser can be located either outdoor or indoor, without any relationship to the operating mode, providing considerable flexibility in system installation. Mode switching between heating and cooling mode operation can be achieved through the switching of hydronic fluid coupling, thus eliminating the need for a refrigerant reversing valve. Furthermore, the condenser and evaporator functions remain the same between the two modes, which allows for more optimal design of each component. Hydronic coupling also allows integration of space-conditioning and water heating systems.

Research Objectives and Approach

The objectives of this research were to investigate the performance of a residential heat pump with microchannel components. Both air-coupled and hydronically coupled systems were developed. For each configuration, components were optimized for the least possible mass, representing low capital cost systems. A corresponding conventional round-tube/flat-fin heat pump model was also developed as a baseline using software available in the literature.

For each system considered, an ideal system model was first developed to obtain state points. The state points from the system model were then used as inputs for component design. The components were designed using appropriate heat transfer and pressure drop models. Both overall lumped and incremental heat exchanger models were developed. After all the components were designed, they were integrated into the system model to investigate system performance.

System performance was evaluated for each configuration over range of expected conditions: in the cooling mode, the ambient temperature was varied from 21.1°C to 40.6°C; and in the heating mode, the ambient temperature was varied from -8.3°C to 18.3°C. Finally, the size, performance, and refrigerant charge for the different heat pump options were compared.

CHAPTER 2. OVERALL SYSTEM MODELING

The heat pump systems investigated in this study were designed to provide a cooling capacity of 10.55 KW (36,000 Btu/hr) in the summer, and a heating load of 15.05 KW in the winter, with an indoor delivered air temperature no less than 43°C. The nominal design conditions for the two operating modes are listed in Table 1. Refrigerant R-22 was used for all the systems investigated in this study.

For the hydronically coupled system, a 50% ethylene-glycol water solution was used as the secondary coolant. The ethylene-glycol water solution was chosen because of its low volatility, relatively low corrosivity, and the ability to lower the freezing point of water. In addition, ethylene-glycol solutions have better thermophysical properties than propylene glycol solutions, especially at lower temperatures. A 50% solution was chosen to prevent the freezing of the hydronic fluid over the range of expected operating temperatures.

A description of the modeling techniques used for the three different configurations studied here follows.

Conventional Round-Tube/Flat Fin System

The ORNL heat pump model developed by Oak Ridge National Laboratory (PUREZ, Mark V, Version—0.95d, 1994) was used to simulate the air-coupled round-tube/flat-fin heat exchanger system. This model is an updated version of the ORNL heat pump model (Fischer and Rice, 1983). It is a FORTRAN program developed to predict the steady-state

Table 1. Nominal Design Conditions

		Ambient Temperature °C (°F)	Relative Humidity Or Humidity Ratio		Air Flow Rate m ³ /s (cfm)
			Inlet	Outlet	
Summer	Outdoor	35 (95)	0.022	0.022	1.74 (3325)
	Indoor	27 (80)	51.1%	100%	0.65 (1200)
Winter	Outdoor	8.3 (47)	72.65 %	100%	1.95 (3325)
	Indoor	21.1 (70)	0.009	0.009	0.67 (1200)

	Refrigerant Side kPa (psi)	Hydronically Water Side kPa (psi)	Air Side kPa (in. H ₂ O)
Allowable Pressure Drop	20.68 (3)	34.47 (5)	0.05 (0.2)

performance of conventional, vapor compression, electrical-driven, air-to-air heat pumps in both heating and cooling modes. It was developed based on the physical principles and generalized correlations to the greatest extent possible. The ORNL heat pump model allows the user to specify the following parameters:

1. System operating conditions.
2. Compressor characteristics.
3. Refrigerant flow control devices.
4. Round-tube/flat-fin heat exchanger parameters.
5. A number of pure and near-azeotropic chlorine-free refrigerants including R-22.
6. Nominal refrigerant pressure drop of auxiliary components.

The model will compute:

1. System capacity and COP.
2. Compressor and fan motor power consumption.
3. Sensible-to-total heat transfer ratio.
4. Heat exchanger outlet air dry and wet-bulb temperatures.
5. Air and refrigerant pressure drops.
6. Overall compressor isentropic and volumetric efficiencies.
7. Heat exchanger effectiveness and UA values.
8. Equivalent capillary tube, TXV and/or short-tube orifice parameters.
9. A summary of the refrigerant-side states throughout the cycle.

The system operation conditions include the desired indoor and outdoor air temperatures and relative humidity and the arrangement of the compressor and fans in the air flow stream, i.e., up or downstream of the heat exchangers. Either a map-based or a loss and efficiency based compressor model can be used. For refrigerant flow control, a capillary tube or thermostatic expansion valve (TXV) or a short-tube orifice, or a fixed value of refrigerant subcooling (or quality) at the condenser outlet can be specified. In this case, the program calculates the equivalent capillary tube, TXV and short-tube orifice parameters.

Tube and fin geometry parameters and air flow rates need to be specified for heat exchanger calculation. The effectiveness-Ntu method is used to calculate dry-coil heat transfer. A modified effective surface temperature approach is used where air

dehumidification occurs. The air-side wet-surface heat transfer coefficient is calculated as a function of the dry-surface heat transfer coefficient. The Dittus-Boelter correlation for fully developed flow (Dittus and Boelter, 1930) is used to calculate the single-phase heat transfer coefficients. The correlation by Traviss (1973) is used to calculate the local condensation heat transfer coefficient, as shown in equations (1) to (5).

$$h_{local} = \begin{cases} k_l \text{Pr Re}^{0.9} \frac{F(X_u)}{D \times F_2} & F(X_u) < 1.0 \\ k_l \text{Pr Re}^{0.9} \frac{F(X_u)^{1.15}}{D \times F_2} & 1.0 < F(X_u) < 15 \end{cases} \quad (1)$$

Where

$$X_u = \left(\frac{\mu_l}{\mu_v} \right)^{0.1} \left(\frac{\rho_v}{\rho_l} \right)^{0.5} \left(\frac{1-x}{x} \right)^{0.9} \quad (2)$$

$$\text{Re} = \frac{GD(1-x)}{\mu_l} \quad (3)$$

$$F(X_u) = 0.15 \left(\frac{1}{X_u} + 2.85 X_u - 0.476 \right) \quad (4)$$

$$F_2 = \begin{cases} 0.707 \text{Pr Re}^{0.5} & \text{Re} < 50 \\ 5.0 \text{Pr} + 5.0 \ln[1.0 + \text{Pr}(0.09636 \text{Re}^{0.585} - 1.0)] & 50 < \text{Re} < 1125 \\ 5.0 \text{Pr} + 5.0 \ln(1.0 + 5.0 \text{Pr}) + 2.5 \ln(0.00313 \text{Re}^{0.812}) & \text{Re} > 1125 \end{cases} \quad (5)$$

The Chaddock and Noerager correlation (1966) is used for the boiling heat transfer coefficient, and the Sthapak correlation (1976) is used for the dry-out region in the evaporator.

Other input parameters include refrigerant type, fan efficiency values for indoor and outdoor fans or the efficiency curve for the outdoor fan, duct size, length and diameter of interconnecting pipes and heat losses from suction, discharge, and liquid lines.

Microchannel Heat Pump Systems

The ORNL heat pump model does not have the capability to simulate air-coupled or hydronically coupled heat pumps that use microchannel tubes. Therefore, models for these systems were developed as part of this study. Both air-coupled and hydronically coupled systems are modeled using Engineering Equation Solver (EES) (Klein and Alvarado, 2000). For both of these systems, thermodynamic analyses of the ideal refrigeration cycle were performed to obtain component state points. Here, an ideal refrigeration cycle means that there is no pressure drop in the heat exchangers and refrigerant lines, which results in a constant condensing and evaporating temperature. Furthermore, the expansion device was assumed to undergo an adiabatic expansion process. To avoid liquid entering the compressor, a superheated state is specified for the evaporator outlet. Similarly, complete condensation in the condenser is ensured by specifying a subcooled outlet state. For the nominal design conditions, condensing and evaporating temperatures are chosen by specifying a closest approach temperature difference (CAT) between the refrigerant and the coolant in each heat exchanger. The compressor isentropic efficiency is calculated using a polynomial equation presented by Jungnickel et al., (1990), where P_1 and P_2 are the condensing and evaporating pressure, respectively.

$$\eta_{isen} = 0.73 + 0.10 \frac{P_2}{P_1} - 0.026 \left(\frac{P_2}{P_1} \right)^2 + 0.0017 \left(\frac{P_2}{P_1} \right)^3 \quad (6)$$

The system heating performance was evaluated over the range of ambient temperatures from -8.3°C to 18.3°C using this model. Then the system was converted to the cooling mode, and system cooling performance was evaluated as the ambient temperature varied from 21.1°C to 40.6°C . The outputs from this ideal system model were used as inputs for component design and optimization where realistic heat exchanger sizes and pressure drops were calculated using the appropriate heat transfer and fluid flow models. Finally, the components were integrated into the overall system.

Air-coupled system

Figure 7 shows the pressure-enthalpy diagram for the air-coupled system. The numbers in the diagram indicate the state points, which are also listed in Table 2. State points [1] through [8] represent the refrigerant states throughout the cycle. The refrigerant enters the

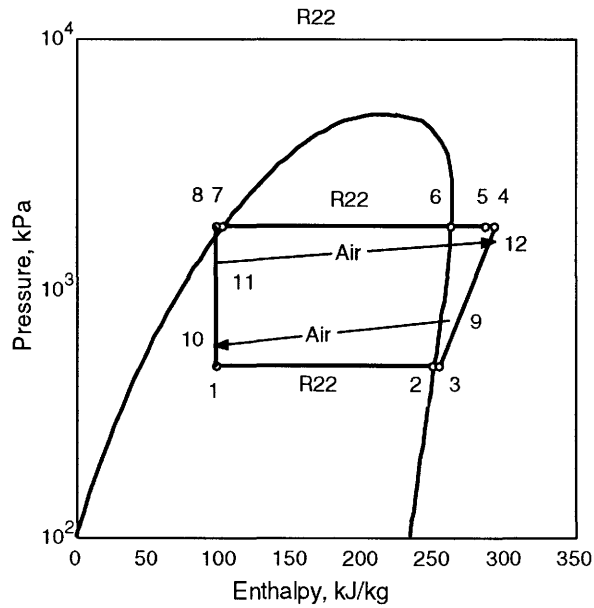


Figure 7. Air-Coupled System P-h Diagram

Table 2. State Points of the Air-Coupled System

State Point No.	Description of State Point
1	Evaporator inlet
2	Evaporator saturated vapor
3	Evaporator superheated outlet
4	Compressor actual outlet
5	Compressor ideal outlet
6	Condenser saturated vapor
7	Condenser saturated liquid
8	Condenser subcooled outlet
9	Evaporator air inlet
10	Evaporator air outlet
11	Condenser air inlet
12	Condenser air outlet

evaporator in a two-phase state at state point [1]. It undergoes evaporation to reach a saturated vapor state [2] and exits the evaporator as a superheated vapor [3]. If isentropic compression is assumed, the ideal compressor outlet state is [5]. However, with an isentropic efficiency specification, the actual compressor outlet is [4]. As the refrigerant flows through the condenser, it reaches the saturated vapor state at [6], is fully condensed at state [7], and

exits as a subcooled liquid at state [8]. An isenthalpic expansion returns this refrigerant to the evaporator inlet state [1]. State point [9] through [12] representing the state conditions for air flow in both evaporator and condenser.

The assumptions used in the air-coupled system model include:

1. Closest approach temperature (CAT) in both condenser and evaporator = 3°C.
2. Evaporator exit superheating degree = 5°C.
3. Condenser exit subcooling degree = 3°C.
4. No pressure drop in heat exchangers and refrigerant lines.
5. Adiabatic expansion process in flow control device.
6. Compressor isentropic efficiency is calculated by equation (6).

Figure 8 shows the sequence of modeling steps for the air-coupled system. With the cooling load and air flow rate provided, the air temperature at state point [10] can be calculated. In this case, the temperature pinch occurs between state points [10] and [1], therefore, the refrigerant temperature at state point 1 can be calculated. With the assumption that there is no pressure drop in the heat exchangers, and the specified superheat, the refrigerant properties at state points [2] and [3], refrigerant mass flow rate (if inlet quality at state [1] is assumed) and evaporating pressure can all be determined. The refrigerant condensing temperature and pressure can be calculated using a similar method. In this case, the temperature pinch occurs between state points [12] and [6]. Due to the unknown heat duty of the condenser, the temperature at state point [12] and isentropic compression must be assumed first to obtain the properties at state points [5], [6], [7] and [8]. From the definition of isentropic efficiency, the refrigerant properties at state point [4], and thus the actual condenser duty can be determined. To close the loop, temperature at state point [12] is calculated from the condenser duty and compared with the assumption until convergence is achieved. In addition, the calculated refrigerant enthalpy at state point [8] is used to replace the assumed evaporator inlet condition.

After the loop is closed, the component UAs required to deliver this performance are computed at the system rating condition. These UAs are then fixed, the CAT constraints are removed and system performance variation over the ambient temperature range is investigated.

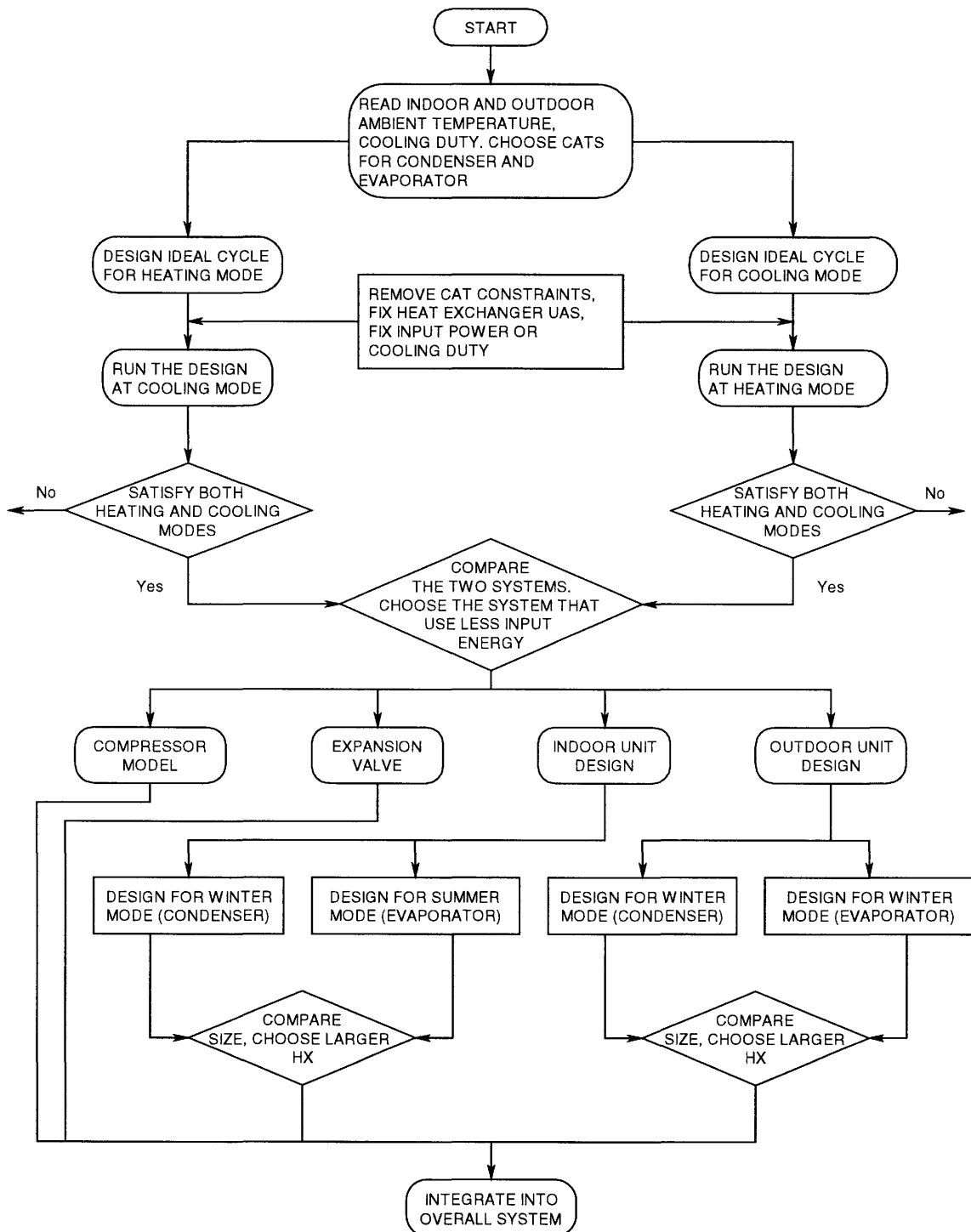


Figure 8. Air-Coupled System Modeling Procedure

System performance for the heating mode can be determined by switching the component UAs and corresponding air flow rates, and adjusting the indoor and outdoor air temperatures. The system that is able to satisfy the requirements in both modes is chosen as the design case.

Detailed heat transfer design of the components was performed in separate programs discussed in a subsequent chapter. It should be noted that when designing the components, refrigerant states at component inlets were estimated using the results from this ideal cycle analysis.

Figures 9 and 10 indicate the effect of CAT and heat exchanger UAs on system COP in heating mode, respectively. As shown in the figures, smaller CATs result in higher COPs, but this will require larger heat exchangers. In Figure 10, the heating mode COP is plotted as a function of condenser UA, while keeping the evaporator UA fixed at 2.283 KW/°C.

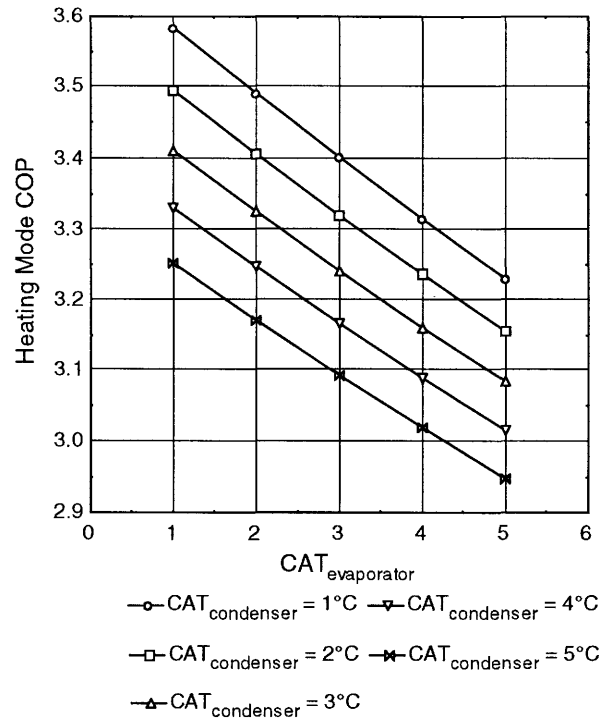


Figure 9. The Effect of CAT on System COP (Heating Mode)

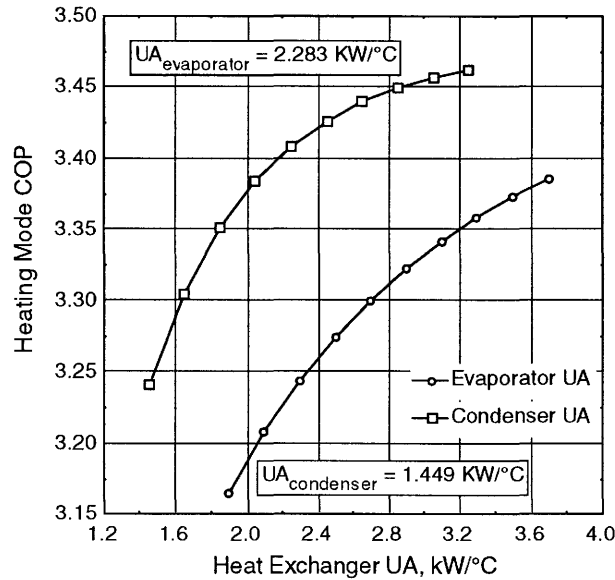


Figure 10. The Effect of CAT on Heat Exchanger UAs (Heating Mode)

Similarly, the heating mode COP is plotted as a function of evaporator UA, while keeping the condenser UA fixed at 1.449 kW/°C. These plots show that system COP first increases sharply as the components UA is increased. This is followed by a much more gradual improvement in COP. Therefore, a CAT of 3°C was chosen for both the condenser and the evaporator to maintain relatively high COPs while keeping the sizes of the heat exchangers acceptable.

Results from the ideal air-coupled heat pump model

The results for the ideal system designed for the cooling mode are listed in Tables 3 and 4. It should be noted that the CAT used for both heat exchangers for this design is 3°C. Table 3 lists the state points, while system performance is listed in Table 4. It can be seen that, for this case, the indoor delivered temperature in the heating mode is not acceptable. Therefore, the system was redesigned using the heating mode requirements as the basis. These results are shown in Table 5 and 6. It can be seen that, for this case, the component UAs are higher, and both heating and cooling requirements are met. It should be noted that, if the compressor input power was kept the same as in heating mode, the cooling capacity of

Table 3. State Points of Air-Coupled System Designed for Cooling Mode

State Point Number	Cooling Mode			Heating Mode		
	Temperature (°C)	Pressure (kPa)	Enthalpy (kJ/kg)	Temperature (°C)	Pressure (kPa)	Enthalpy (kJ/kg)
<i>Refrigerant State Points</i>						
1	11.31	707.41	96.72	1.42	520.73	89.32
2	11.31	707.41	253.85	1.42	520.73	250.46
3	16.31	707.41	257.69	6.42	520.73	254.10
4	68.76	1718.68	284.38	67.34	1502.32	286.21
5	64.13	1718.68	280.21	61.50	1502.32	281.16
6	44.77	1718.68	261.87	39.18	1502.32	261.01
7	44.77	1718.68	100.66	39.18	1502.32	93.18
8	41.77	1718.68	96.72	36.18	1502.32	89.32
<i>Air State Points</i>						
9	27.00	101.33	56.24	8.30	101.33	20.74
10	14.31	101.33	40.11	3.73	101.33	16.14
11	35.00	101.33	91.65	21.10	101.33	44.09
12	41.77	101.33	98.74	36.75	101.33	60.10

Table 4. Performance of Air-Coupled System Designed for Cooling Mode

	Cooling Mode	Heating Mode
$Q_{\text{evaporator}}$ (KW)	10.55	8.98
$Q_{\text{condenser}}$ (KW)	12.30	10.72
$\text{COP}_{\text{cooling}}$	3.96	
$\text{COP}_{\text{heating}}$		4.02
$\text{UA}_{\text{evaporator}}$ (KW/°C)	1.38	2.14
$\text{UA}_{\text{condenser}}$ (KW/°C)	2.14	1.38
Compressor Power (KW)	2.66	2.66
Delivered Temperature (°C)	14.31	36.75
Refrigerant Flow Rate (kg/s)	0.06554	0.05447

the system is higher than necessary. Thus, for the cooling mode, compressor input power was decreased to keep the system cooling capacity at 10.55 KW (36,000 Btu/hr).

Changing the ambient temperature will also affect the performance of the system. Once the system was designed as described above, its performance was evaluated as a function of ambient temperature in both modes. For these analyses, the UA values for both heat exchangers were kept constant at the values required for a CAT = 3°C at the design case (heating mode, see Table 6). In addition, the compressor power was kept constant at the

Table 5. State Points of Air-Coupled System Designed for Heating Mode

State Point Number	Cooling Mode			Heating Mode		
	Temperature (°C)	Pressure (kPa)	Enthalpy (kJ/kg)	Temperature (°C)	Pressure (kPa)	Enthalpy (kJ/kg)
<i>Refrigerant State Points</i>						
1	11.62	714.03	96.27	-0.09	495.84	98.38
2	11.62	714.03	253.95	-0.09	495.84	249.92
3	16.62	714.03	257.80	4.91	495.84	253.52
4	68.05	1704.87	283.95	79.12	1769.19	292.89
5	63.51	1704.87	279.86	71.73	1769.19	286.32
6	44.43	1704.87	261.82	46.00	1769.19	262.02
7	44.43	1704.87	100.20	46.00	1769.19	102.33
8	41.43	1704.87	96.27	43.00	1769.19	98.38
<i>Air State Points</i>						
9	27.00	101.33	56.24	8.30	101.33	20.74
10	14.31	101.33	40.11	2.91	101.33	14.61
11	35.00	101.33	91.65	21.10	101.33	44.09
12	41.75	101.33	98.71	43.00	101.33	66.49

Table 6. Performance of Air-Coupled System Designed for Heating Mode

	Cooling Mode	Heating Mode
$Q_{evaporator}$ (KW)	10.55	11.97
$Q_{condenser}$ (KW)	12.26	15.00
$COP_{cooling}$	4.05	
$COP_{heating}$		3.24
$UA_{evaporator}$ (KW/°C)	1.45	2.28
$UA_{condenser}$ (KW/°C)	2.28	1.45
Compressor Power (KW)	2.60	4.63
Delivered Temperature (°C)	14.31	43.00
Refrigerant Flow Rate (kg/s)	0.06532	0.07714

design case value as the ambient temperature was varied. Figures 11 - 14 show the effects of outdoor ambient temperature on heating and cooling mode COPs. In the heating mode, as the outdoor ambient temperature increases, the COP increases, with a corresponding increase in the indoor delivered temperature and system heating capacity. However, in the cooling mode, as the ambient temperature increases, the indoor delivered temperature increases, while the system COP and cooling capacity decrease.

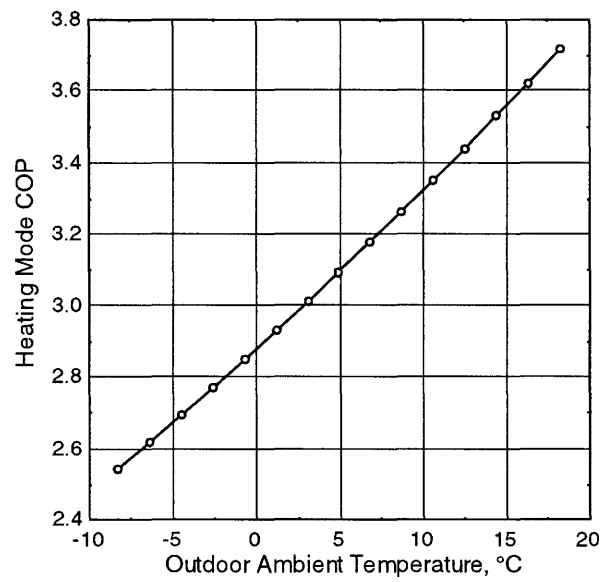


Figure 11. Effect of Ambient Temperature on Heating Mode COP (Air-Coupled System)

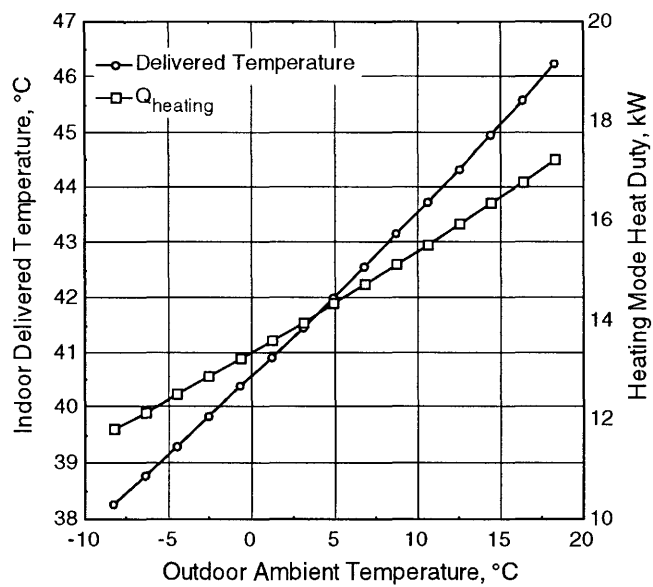


Figure 12. Effect of Ambient Temperature on Heating Mode Performance (Air-Coupled System)

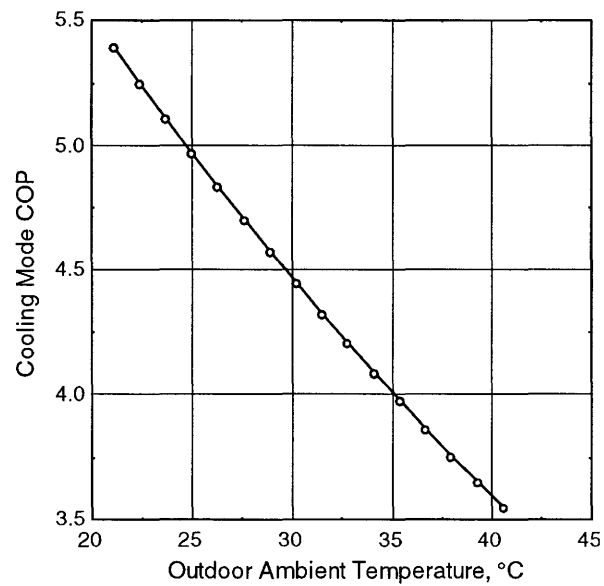


Figure 13. Effect of Ambient Temperature on Cooling Mode COP (Air-Coupled System)

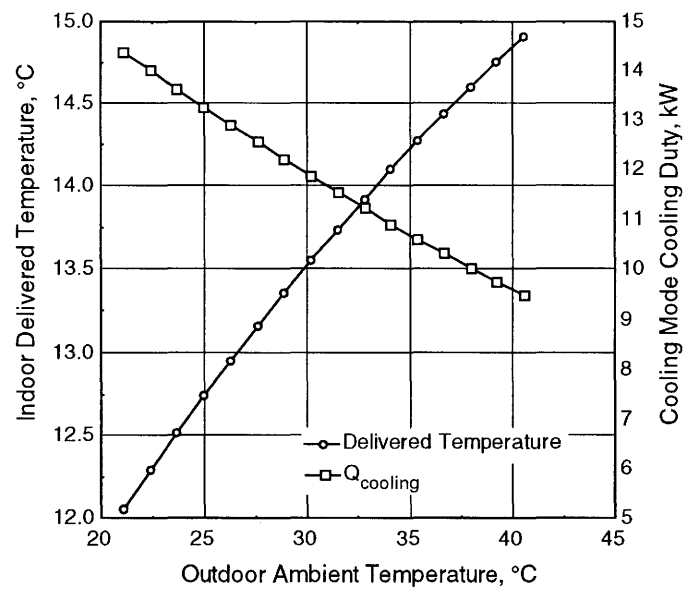


Figure 14. Effect of Ambient Temperature on Cooling Mode Performance (Air-Coupled System)

Hydronically coupled system

Similar analyses were also conducted for the hydronically coupled system. The P-h diagram for this system is shown in Figure 15. Again, the numbers in diagram indicate the state points used in system. The modeling procedure for the hydronically coupled system is similar to that used in the air-coupled system. But unlike in the air-coupled system, the condenser and evaporator do not change function between the two modes. However, the functions of the indoor and outdoor heat exchangers are different between the two modes. Therefore, the system was designed to meet the requirements for these components for the operating mode that required the larger UA value.

The assumptions used to design the hydronically coupled system were similar to those used for the air-coupled system and are listed below

1. The closest approach temperature (CAT) for both the refrigerant-to-hydraulic fluid condenser, and the refrigerant-to-hydraulic fluid evaporator was chosen to be 1.5°C. The reason for this small CAT is that an additional temperature difference between the refrigerant and air is introduced by the intermediate hydronic loop. However,

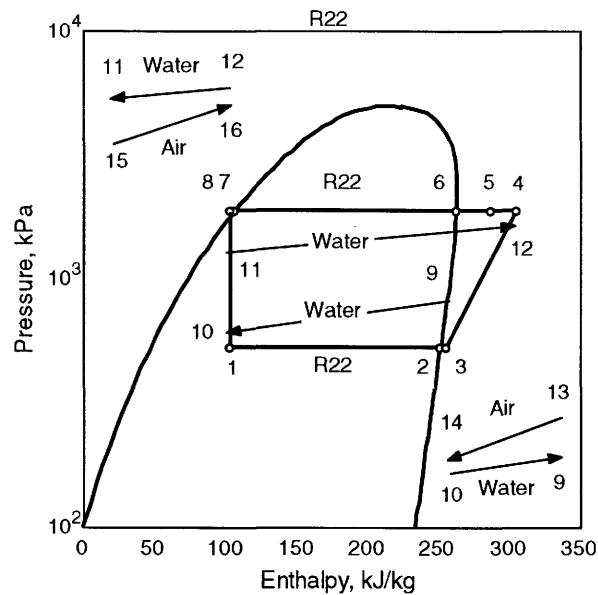


Figure 15. Hydronically Coupled System P-h Diagram

the total temperature difference available from refrigerant to air is limited. Therefore, the choice of a small CAT for the hydronically coupled condenser and evaporator will leave the larger portion of the available refrigerant-to-air ΔT for the hydronic fluid-to-air heat exchange, which has a relatively low U value. It should be noted that due to the high refrigerant and hydronic fluid heat transfer coefficients and the pure counter flow arrangement, such low CATs can be achieved without very large hydronic fluid-to-refrigerant heat exchangers.

2. CAT for the hot side c is 3.3°C.
3. CAT for the cold side air-to-hydronic fluid heat exchanger is 3.3°C.
4. Evaporator exit superheat is 5°C.
5. Condenser exit subcooling is 3°C.
6. No pressure drop in heat exchangers and refrigerant lines.
7. Adiabatic expansion process in flow control device.
8. Compressor isentropic efficiency is calculated using equation (6).

Results from the ideal hydronically coupled heat pump model

Similar to the air-coupled system, the hydronically coupled system was designed for both cooling and heating modes. The results are listed in Tables 7 to 10. State points [13]-[14] and [15]-[16] refer to cold side air-to-hydronic fluid heat exchanger inlet and outlet, and hot side air-to-hydronic fluid heat exchanger inlet and outlet, respectively. Again, if the system is designed for the cooling mode, the indoor delivered air temperature is lower than the required 43°C when the system operates in the heating mode. However, both cooling and heating requirements are met if the system is designed for the heating mode. When operating in cooling mode, the compressor input power is decreased to provide the required 10.55 KW cooling capacity.

The performance of the hydronically coupled system calculated using these assumptions is shown in Figures 16 and 17 for the heating and cooling modes, respectively. The results from these system-level models were used to design components for both types of heat pumps. These component designs are discussed in the following chapter.

Table 7. State Points of Hydronically Coupled System Designed for Cooling Mode

State Point Number	Cooling Mode			Heating Mode		
	Temperature (°C)	Pressure (kPa)	Enthalpy (kJ/kg)	Temperature (°C)	Pressure (kPa)	Enthalpy (kJ/kg)
Refrigerant State Points						
1	9.51	670.18	99.35	-0.24	493.38	91.96
2	9.51	670.18	253.26	-0.24	493.38	249.86
3	14.51	670.18	257.06	4.76	493.38	253.46
4	72.83	1799.31	286.88	71.74	1577.39	288.98
5	67.70	1799.31	282.23	65.19	1577.39	283.28
6	46.72	1799.31	262.11	41.19	1577.39	261.34
7	46.72	1799.31	103.31	41.19	1577.39	95.84
8	43.72	1799.31	99.35	39.19	1577.39	91.96
Hydronic Fluid State Points						
9	16.93			6.17		
10	11.01			1.04		
11	38.29			33.74		
12	45.22			39.87		
Air State Points						
13	27.00	101.33	56.24	8.30	101.33	20.74
14	14.31	101.33	40.11	3.71	101.33	16.09
15	35.00	101.33	91.65	21.10	101.33	44.09
16	41.91	101.33	98.87	37.25	101.33	94.00

Table 8. Performance of Hydronically Coupled System Designed for Cooling Mode

	Cooling Mode	Heating Mode
$Q_{evaporator}$ (KW)	10.55	9.07
$Q_{condenser}$ (KW)	12.55	11.06
Q_{cold} (KW)	10.55	9.07
Q_{hot} (KW)	12.55	11.06
$COP_{cooling}$	3.47	
$COP_{heating}$		3.64
$UA_{evaporator}$ (KW/°C)	2.85	2.85
$UA_{condenser}$ (KW/°C)	3.13	3.13
$UA_{cold, air-hyd HX}$ (KW/°C)	1.74	3.80
$UA_{hot, air-hyd HX}$ (KW/°C)	3.80	1.74
Compressor Power (KW)	3.04	3.04
Delivered Temperature (°C)	14.31	37.25
Refrigerant Flow Rate (kg/s)	0.06690	0.05616

Table 9. State Points of Hydronically Coupled System Designed for Heating Mode

State Point Number	Cooling Mode			Heating Mode		
	Temperature (°C)	Pressure (kPa)	Enthalpy (kJ/kg)	Temperature (°C)	Pressure (kPa)	Enthalpy (kJ/kg)
Refrigerant State Points						
1	9.83	676.67	100.30	-3.07	449.36	100.80
2	9.83	676.67	253.36	-3.07	449.36	248.81
3	14.83	676.67	257.18	1.93	449.36	252.36
4	73.65	1829.15	287.21	84.88	1844.70	297.01
5	68.51	1829.15	282.52	75.85	1844.70	288.97
6	47.43	1829.15	262.18	47.79	1844.70	262.22
7	47.43	1829.15	104.28	47.79	1844.70	104.78
8	44.43	1829.15	100.30	44.79	1844.70	100.80
Hydronic Fluid State Points						
9	17.12			5.00		
10	11.21			-1.57		
11	39.23			38.00		
12	46.17			46.29		
Air State Points						
13	27.00	101.33	56.24	8.30	101.33	20.74
14	14.31	101.33	40.11	3.02	101.33	14.80
15	35.00	101.33	91.65	21.10	101.33	44.09
16	41.92	101.33	98.89	43.00	101.33	66.49

Table 10. Performance of Hydronically Coupled System Designed for Heating Mode

	Cooling Mode	Heating Mode
$Q_{\text{evaporator}}$ (KW)	10.55	11.59
$Q_{\text{condenser}}$ (KW)	12.57	15.00
Q_{cold} (KW)	10.55	11.59
Q_{hot} (KW)	12.57	15.00
$\text{COP}_{\text{cooling}}$	3.43	
$\text{COP}_{\text{heating}}$		2.88
$\text{UA}_{\text{evaporator}}$ (KW/°C)	2.97	2.97
$\text{UA}_{\text{condenser}}$ (KW/°C)	3.40	3.40
$\text{UA}_{\text{cold,air-hyd HX}}$ (KW/°C)	1.80	2.97
$\text{UA}_{\text{hot,air-hyd HX}}$ (KW/°C)	2.97	1.80
Compressor Power (KW)	3.08	5.20
Delivered Temperature (°C)	14.31	43.00
Refrigerant Flow Rate (kg/s)	0.06726	0.07647

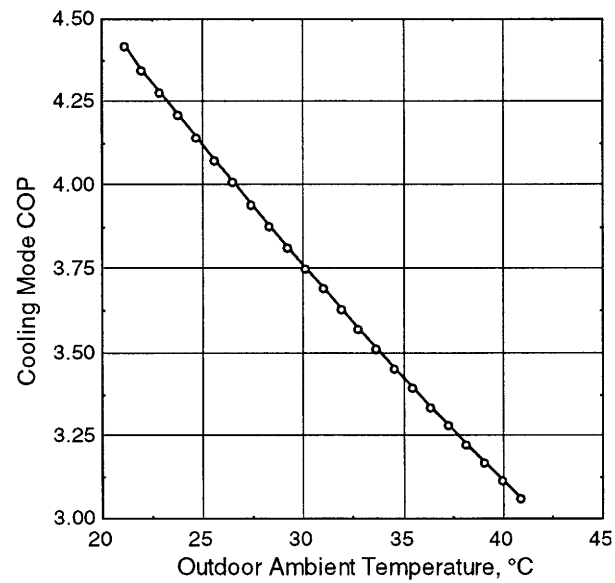


Figure 16. Effect of Ambient Temperature on Cooling Mode Performance (Hydronically Coupled System)

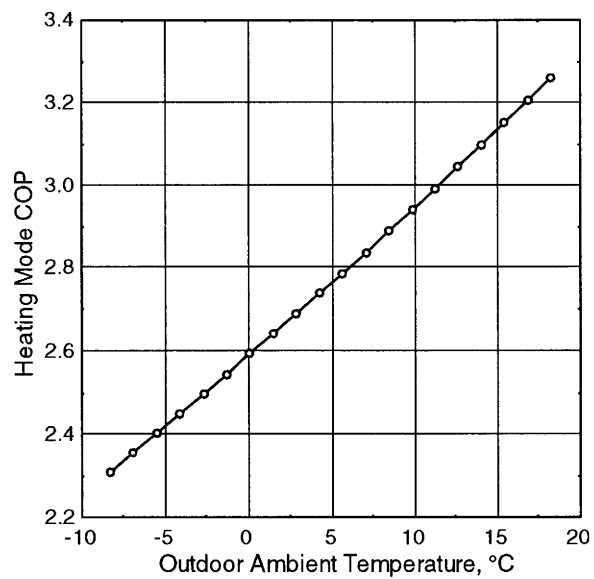


Figure 17. Effect of Ambient Temperature on Heating Mode Performance (Hydronically Coupled System)

CHAPTER 3. HEAT EXCHANGER MODELING

This chapter discusses the design procedures for all the heat exchangers for both the air-coupled and hydronically coupled systems. It should be noted that in the hydronically coupled system, a 50% ethylene-glycol water solution was used as the hydronic fluid.

Overview of Heat Exchanger Modeling Procedures

The heat exchangers to be modeled in this study are shown in Table 11. The evaporator and condenser were divided into single-phase and two-phase regions. That is, the evaporator was divided into evaporating and superheating sections; the condenser was divided into desuperheating, condensing and subcooling sections. Hydronic fluid side of the refrigerant-to-hydronic fluid and hydronic fluid-to-air heat exchangers were all modeled using single-phase correlations. Depending on whether dehumidification will occur or not, air-side heat transfer was categorized as dry-surface heat transfer or wet-surface heat transfer. Below are the design procedures for air-coupled and hydronically coupled heat exchangers.

If no moisture is removed from the air (sensible heating or cooling only), for instance, condenser and radiator, a dry-surface model can be used. However, in cooling applications, it is more common that dehumidification of the air also occurs. With dehumidification, the air-side surface is wet and there is a transfer of latent heat because of condensation. Since water-vapor transfer is not dependent upon temperature difference alone, the *LMTD* (logarithmic mean temperature) method is not valid. Instead of a temperature difference, the driving potential for heat transfer in this case is the enthalpy difference. The *UA* value is evaluated based on the logarithmic mean enthalpy difference, Δh_m .

The design of each heat exchanger was initiated with an assumed geometry. Thus, for

Table 11. Heat Exchangers Modeled in This Study

Air-Coupled System	Hydronically Coupled System
Air-to-refrigerant condenser	Hydronic fluid-to-refrigerant condenser
Air-to-refrigerant evaporator	Hydronic fluid-to-refrigerant evaporator
	Indoor air-to-hydronic fluid heat exchangers
	Outdoor air-to-hydronic fluid heat exchangers

air-coupled heat exchangers, tube dimensions, pass arrangement, fin and louver parameters, and overall heat exchanger dimensions were assumed. For hydronically coupled heat exchangers, tube dimensions, pass arrangement, and overall heat exchanger dimensions for both sides were assumed. These parameters are shown in Tables 12 and 13 for air-coupled

Table 12. Input Geometry Features and Properties for Air-Coupled Heat Exchangers

Tube Side	Center/Fin	Louver
Outside tube height, t_{ho}	Center (fin) height, c_h	Louver width, l_w
Outside tube width, t_{wo}	Center depth, c_w , usually $c_w = t_{wo}$	Louver length, l_l
Tube wall thickness, t_t	Fin thickness, f_t	Louver angle, θ
Number of strengthening webs, N_w	Fin pitch, f_p	
Web thickness, w_t	Number of centers per pass, N_c	
Number of tubes per pass, N_t	Thermal conductivity of fin k_f	
Tube wall roughness, ε_t		
Number of passes, N_r		
Thermal conductivity of tube wall k_t		

Table 13. Input Geometry Features and Properties for Hydronically Coupled Heat Exchangers

Refrigerant Side	Glycol Water Side
Outside tube height, $t_{ho,r}$	Outside tube height, $t_{ho,h}$
Outside tube width, $t_{wo,r}$	Outside tube width, $t_{wo,h}$
Tube wall thickness, $t_{t,r}$	Tube wall thickness, $t_{t,h}$
Number of strengthening webs, $N_{w,r}$	Number of strengthening webs, $N_{w,h}$
Web thickness, $w_{t,r}$	Web thickness, $w_{t,h}$
Number of tubes per pass, $N_{t,r}$	Number of tubes per pass, $N_{t,h}$
Tube wall roughness, $\varepsilon_{t,r}$	Tube wall roughness, $\varepsilon_{t,h}$
Thermal conductivity of refrigerant-side tube wall $k_{t,r}$	Thermal conductivity of glycol-water side tube wall $k_{t,h}$

and hydronically coupled heat exchangers, respectively. With the initial configuration established, geometric parameters such as cross-sectional areas for both sides, and direct and indirect surface areas for both sides were calculated. Design conditions for the two fluids in each heat exchanger, which were obtained from the system model described in the previous chapter, were then used to compute the heat transfer and pressure drop-related variables. These input design conditions for air-coupled and hydronically coupled heat exchangers are shown in Table 14 and 15, respectively. Details of these calculations are provided in a subsequent sub-section. Once the heat transfer coefficients for each side are determined, the overall UA was calculated, including a consideration of the relevant fin efficiencies and surface areas.

It should be noted that, as appropriate, heat transfer and pressure drop analyses were

Table 14. Design Conditions for Air-Coupled Heat Exchangers

Tube Side	
Refrigerant-to Air Heat Exchanger	Hydronic fluid-to Air Heat Exchanger
R22 inlet temperature $T_{r,in}$	Glycol water inlet temperature $T_{h,in}$
R22 inlet pressure $P_{r,in}$ or quality $x_{r,in}$	Glycol water inlet pressure $P_{h,in}$ (optional since the properties of glycol water is not a function of pressure)
R22 mass flow rate \dot{m}_r	Glycol water flow rate, \dot{m}_h or Vol_h
R22 outlet temperature $T_{r,out}$, quality $x_{r,out}$, or superheat ΔT_{sup} /subcooled ΔT_{sub} or required heat duty Q	Allowable Glycol Water Side Pressure Drop ΔP_h
Allowable tube side pressure drop ΔP_r	
Air Side	
Air inlet temperature $T_{a,in}$	
Air inlet pressure $P_{a,in}$	
Air inlet humidity ratio or relative humidity	
Air flow rate \dot{m}_a or Vol_a	
Allowable air side pressure drop ΔP_a	

Table 15. Design Conditions for Hydronically Coupled Heat Exchangers

Refrigerant Side	Hydronic fluid-to Air Heat Exchanger
R22 inlet temperature $T_{r,in}$	Glycol water inlet temperature $T_{h,in}$
R22 inlet pressure $P_{r,in}$ or quality $x_{r,in}$	Glycol water inlet pressure $P_{h,in}$ (optional since the properties of glycol water is not a function of pressure)
R22 mass flow rate, \dot{m}_r	Glycol water flow rate, \dot{m}_h or Vol_h
R22 outlet temperature $T_{r,out}$, quality $x_{r,out}$, or superheat ΔT_{sup} /subcool ΔT_{sub} degree or required heat duty, Q	Allowable Glycol Water Side Pressure Drop ΔP_h
Allowable Refrigerant Side Pressure Drop ΔP_r	

conducted either by treating the whole heat exchanger as one segment, or by splitting portions of the heat exchanger into multiple segments to yield higher accuracies. Thus, a heat exchanger used for rejecting heat from the hydronic fluid to air was treated as one lumped entity, because of the minimal variation in fluid properties, heat transfer coefficients and pressure drop per unit length along the length of the heat exchanger. However, refrigerant-to-air and refrigerant-to-hydronic fluid heat exchangers were analyzed at two levels of detail:

1. Coarse analysis:

- (a) Condenser divided into three segments, desuperheating, condensing and subcooling, with different (single-phase and two-phase) calculations conducted for each segment.
- (b) Evaporator divided into two segments, evaporating, and superheating, with different (single-phase and two-phase) calculations conducted for each segment.

2. Fine analysis:

The two-phase portions of the condenser and evaporator were further subdivided into finer increments of equal quality change to better represent the considerable variations in heat transfer coefficient and pressure drop with the change in quality along the length of the heat exchanger.

It should be noted that for the air-coupled evaporator and the cold hydronic fluid-to-air heat exchanger, two different procedures were used for the air-side of the evaporator (as stated above) based on whether or not dehumidification occurred in the heat exchanger.

Once the UA for the heat exchanger was calculated, the heat duty and pressure drop were computed and compared with the required load and the allowable pressure drops. If these were not met, the geometry was modified until heat load and pressure drop criteria were met. In addition, for each heat exchanger, several different configurations that met these criteria were designed, to find the minimum heat exchanger mass option. The details of each phase of these calculations are presented below.

Geometry calculation

This section discusses the calculation of the geometry of the microchannel flat tubes and louvered fins.

Tube side

Accounting for the fact that the ends of the rectangular tube are semi-circles with a diameter equal to the tube height, (Figure 18) the inside cross-sectional area, A_t , of each tube without the strengthening webs is calculated as follows:

$$A_t = t_{hi}(t_{wi} - t_{hi}) + \frac{\pi}{4} t_{hi}^2 \quad (7)$$

Where t_{hi} and t_{wi} are the tube inner height and width, respectively. The total tube inside free flow area, $A_{f,t}$ is then calculated using the following equation:

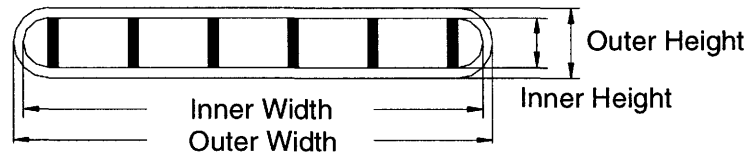


Figure 18. Geometric Details of A Microchannel Tube

$$A_{f,t} = A_t - N_w t_{hi} w_t \quad (8)$$

Where N_w and w_t are number of strengthening webs and the thickness of the webs, respectively. The inner perimeter per_t and hydraulic diameter $D_{h,t}$ are given by:

$$per_t = \pi t_{hi} + 2(t_{wi} - t_{hi} - N_w w_t) + 2t_{hi} N_w \quad (9)$$

$$D_{h,t} = \frac{4A_{f,t}}{per_t} \quad (10)$$

The tube-side direct and indirect heat transfer areas $A_{d,t}$ and $A_{id,t}$ per tube per unit length can be calculated as follows:

$$A_{d,t} = 2(t_{wi} - t_{hi}) + \pi t_{hi} - 2N_w w_t \quad (11)$$

$$A_{id,t} = 2N_w t_{hi} \quad (12)$$

Considering the strengthening web as a fin with one-half the height of webs as the length of the fin, the tube-side fin efficiency $\eta_{f,t}$ and tube-side effective heat transfer area $A_{eff,t}$ can be calculated by the following equations:

$$\eta_{f,t} = \frac{\tanh\left[\sqrt{\frac{2h_t}{k_t w_t}} \frac{t_{hi}}{2}\right]}{\left[\sqrt{\frac{2h_t}{k_t w_t}} \frac{t_{hi}}{2}\right]} \quad (13)$$

$$A_{eff,t} = A_{d,t} + \eta_{f,t} A_{id,t} \quad (14)$$

Where h_t and k_t are tube side heat transfer coefficient and tube thermal conductivity, respectively.

Air side

As shown in Figure 19, the total core face area, A_c , is given by:

$$A_c = (N_i t_{ho} + N_c c_h) L_t \quad (15)$$

Where t_{ho} and c_h are tube outer height and center (fin) height, respectively. N_c is the number of centers; L_t is the tube length per pass. The air side flow area blocked by fins, $A_{b,a}$, and total free flow area, $A_{f,a}$, are given by:

$$A_{b,a} = \frac{L_t}{f_p} [c_h f_t + (f_p - f_t) f_t] N_c \quad (16)$$

$$A_{f,a} = A_c - (A_{b,a} + N_t t_{ho} L_t) \quad (17)$$

Where f_p and f_t are the fin pitch and fin thickness, respectively. The fin-side perimeter per_a and hydraulic diameter $D_{h,a}$ are calculated by the following equations:

$$per_a = 2N_c \left[\frac{L_t}{f_p} (c_h - f_t) + \left(L_t - \frac{L_t}{f_p} f_t \right) \right] + 2N_c c_h \quad (18)$$

$$D_{h,a} = \frac{4A_{f,a}}{per_a} \quad (19)$$

The fin-side heat transfer area calculation is also based on a per center per unit tube length basis. The fin-side direct and indirect heat transfer area $A_{d,a}$ and $A_{id,a}$ can be calculated as follows (Figure 20):

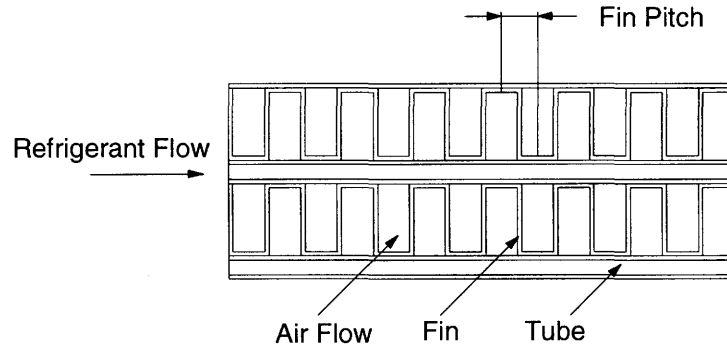


Figure 19. Geometric Details of A Multilouver Fin

$$A_{d,a} = 2(t_{wo} - t_{ho}) \left(1 - \frac{f_t}{f_p} \right) + \pi_{ho} \quad (20)$$

$$A_{id,a} = 2c_w \frac{1}{f_p} (c_h - f_t) \quad (21)$$

The fin efficiency $\eta_{f,a}$ and air-side effective heat transfer area $A_{eff,a}$ can be calculated from the following equations:

$$\eta_{f,a} = \frac{\tanh \left[\sqrt{\frac{2h_a}{k_f} \frac{c_h}{f_t} \frac{1}{2}} \right]}{\left[\sqrt{\frac{2h_a}{k_f} \frac{c_h}{f_t} \frac{1}{2}} \right]} \quad (22)$$

$$A_{eff,a} = A_{d,a} + \eta_{f,a} A_{id,a} \quad (23)$$

Where h_a and k_f are the air-side heat transfer coefficient and fin thermal conductivity, respectively.

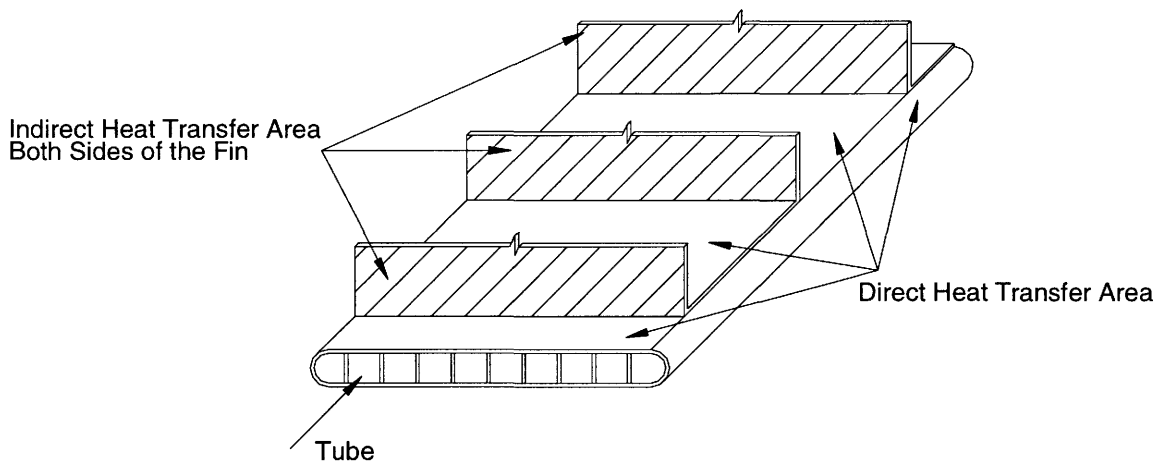


Figure 20. Fin-Side Heat Transfer Area

Heat transfer and pressure drop calculations

Single-phase heat transfer and pressure drop

The heat transfer and pressure drop for the hydronic fluid and single-phase refrigerant flow through the rectangular cross section ports in the tubes were calculated using correlations for round tubes with modifications to account the non-circular cross section. According to the Handbook of Single-Phase Convective Heat Transfer (Kakac *et al.*, 1987), the critical Reynolds number in a rectangular duct can be calculated using the following equation (Bhatti and Shah, 1987):

$$\text{Re}_{crit} = \frac{4650}{\text{velocity ratio}} \quad (24)$$

Where *velocity ratio* is the ratio of the maximum and mean velocities in laminar flow in a rectangular duct. An approximate expression proposed by Puday (1949) is used to calculate this *velocity ratio*.

$$\text{velocity ratio} = \frac{V_{mean}}{V_{max}} = \left(\frac{m+1}{m} \right) \left(\frac{n+1}{n} \right) \quad (25)$$

Parameter m and n can be determined using equations (26) and (27).

$$n = 2 \quad \text{when } \alpha < \frac{1}{3}, \text{ or } \quad n = 2 + 0.3 \left(\alpha - \frac{1}{3} \right) \quad \text{when } \alpha \geq \frac{1}{3} \quad (26)$$

$$m = 1.7 + 0.5\alpha^{-1.4} \quad (27)$$

Where the flat tube height/width ratio can be calculated as follows:

$$\alpha = \frac{\text{tube height}}{\text{tube width}} \quad (28)$$

Once the critical Reynolds number is calculated, the appropriate flow regime can be identified. For laminar flow, ($\text{Re} < \text{Re}_{crit}$), the Darcy friction factor and Nusselt number can be computed using the following equations:

$$f_t = 96 \left[\frac{1 - 0.8765\alpha + 1.2753\alpha^2 - 1.3086\alpha^3 + 0.5765\alpha^4}{\text{Re}} \right] \quad (29)$$

$$Nu_t = 8.325(1 - 2.0241\alpha + 3.0853\alpha^2 - 2.4765\alpha^3 + 1.0578\alpha^4 - 0.1861\alpha^5) \quad (30)$$

where the Reynolds number is based on tube hydraulic diameter, $Re = \frac{\rho V D_h}{\mu}$. For turbulent flow ($Re \geq Re_{crit}$), Shah and Bhatti (1987) recommend the following multiplier to the circular-tube friction factor.

$$f_t = (1.0875 - 0.1125\alpha) f_{circ} \quad (31)$$

Where Churchill equation (1977a and b) was used to compute the circular tube Darcy friction factor.

$$f_{circ} = 8 \left[\left(\frac{8}{Re} \right)^{12} + \frac{1}{\left(\left[2.457 \ln \left(\frac{1}{(7/Re)^{0.9} + 0.27\epsilon} \right) \right]^{16} + \left[\frac{37530}{Re} \right]^{16} \right)^{1.5}} \right]^{1/12} \quad (32)$$

Nusselt numbers in turbulent flow are well approximated by the following circular tube correlation proposed by Churchill (1977a and b).

$$Nu_t^{10} = 4.364^{10} + \left[\frac{\exp\left(\frac{2200 - Re}{365}\right)}{4.364^2} + \frac{1}{\left(6.3 + \frac{0.079(f_{circ}/8)^{1/2} Re Pr_t}{(1 + Pr_t^{4/5})^{5/6}} \right)^2} \right]^{-5} \quad (33)$$

With $h_t = \frac{Nu_t k_t}{D_{h,t}}$, the tube-side heat transfer coefficient can be calculated. The single-phase pressure drop was calculated using the equation below. Liquid or vapor properties were used as appropriate.

$$\Delta P_t = \frac{1}{2} f_t \rho V^2 \frac{L_t}{D_{h,t}} \quad (34)$$

Two-phase Heat transfer coefficient and pressure drop

There are no correlations in the literature to calculate two-phase heat transfer and pressure drop through non-circular microchannels. Therefore, for this study, heat transfer coefficients and pressure drop through the rectangular ports in the tubes were calculated using circular tube correlations. The applicability of these correlations to the geometries under investigation is not well established because of the potentially different fluid flow phenomena at such small scales. However, the heat exchanger sizes predicted using this approach may not be very sensitive to the validity of these correlations because in many of the heat exchangers under consideration, the refrigerant side does not present the governing thermal resistance. The Chen correlation (1966) was used to calculate the boiling heat transfer coefficient in the evaporator. Chen argued that the heat transfer coefficient for saturated convective boiling is equal to the sum of a microscopic (nucleate boiling) contribution and a macroscopic (bulk convective) contribution. Thus:

$$h_{p,boiling} = h_{NB} + h_{FC} \quad (35)$$

where h_{NB} and h_{FC} are the nucleate boiling and forced convective heat transfer coefficient components, respectively.

$$h_{NB} = S \times h_{FZ} \quad (36)$$

$$h_{FC} = F \times h_l \quad (37)$$

where h_{FZ} is the Forster-Zuber nucleate boiling coefficient calculated as follows.

$$h_{FZ} = 0.00122 \Delta T_{sat}^{0.24} \Delta P_{sat}^{0.75} C p_l^{0.45} \rho_l^{0.49} \frac{k_l^{0.79}}{\sigma^{0.5} h_{LG}^{0.24} \mu_l^{0.29} \rho_v^{0.24}} \quad (38)$$

Here, ΔT_{sat} and ΔP_{sat} are refrigerant saturation temperature and pressure differences, respectively. $C p_b$, ρ_b , ρ_v , k_b , μ_b , σ and h_{LG} are refrigerant liquid specific heat, liquid density, vapor density, thermal conductivity, kinetic viscosity, surface tension and latent heat, respectively. h_l in equation (37) is the heat transfer coefficient for liquid phase flowing alone:

$$h_l = 0.023 \frac{k_l}{D_h} \text{Re}_l^{0.8} \text{Pr}_l^{1/3} \quad (39)$$

In equation (36), S is a suppression factor to account for the reduction in the heat transfer coefficient due to the suppression of nucleation sites in the presence of convective boiling. S is related to the two-phase Reynolds number Re as follows:

$$\text{Re} = \text{Re}_l \times F^{1.25} \quad (40)$$

$$F = 2.35 \left(\frac{1}{X_{tt}} + 0.213 \right)^{0.736} \quad (41)$$

$$S = \frac{1}{1 + 2.53 \times 10^{-6} \text{Re}^{1.17}} \quad (42)$$

where Re_l in equation (40) is the Reynolds number for the liquid phase flowing alone in the channel, $\text{Re}_l = \frac{G(1-x)D_h}{\mu}$. G and x are refrigerant mass flux and quality, respectively. X_{tt} in Equation (41) is the Lockhart-Martinelli parameter, which is given by the Blasius equation:

$$X_{tt} = \left(\frac{1-x_{avg}}{x_{avg}} \right)^{0.87} \left(\frac{\rho_v}{\rho_l} \right)^{0.5} \left(\frac{\mu_l}{\mu_v} \right)^{0.125} \quad (43)$$

Shah's empirical correlation (Shah, 1989) using data from ten fluids for the mass flux range $11 \leq G_t \leq 211 \text{ kg/m}^2\text{s}$ ($8110 \leq G_t \leq 155600 \text{ lb}_m/\text{hr} \cdot \text{ft}^2$) was used to calculate the condensation heat transfer coefficient, as follows:

$$h_{tp,condensation} = 0.023 \frac{k_l}{D_{h,t}} \text{Re}_{lo}^{0.8} \text{Pr}_l^{0.4} \left[(1-x)^{0.8} + \frac{3.8x^{0.76}(1-x)^{0.04}}{(P_{sat}/P_{crit})^{0.38}} \right] \quad (44)$$

This correlation was employed because the mass flux of interest is within its range of applicability. Here, the subscript tp and l refer to two-phase and liquid properties, respectively. Re_{lo} refers to Reynolds number evaluated assuming that the entire flow is in the liquid phase.

The tube-side pressure drop in two-phase flow was calculated using the following equation, where subscript l and v refer to liquid and vapor, respectively:

$$\Delta P_t = \frac{G_t^2}{2 \rho_v D_{h,t}} f_v x^2 \Phi^2 L_t + G_t^2 \left[\left(\frac{x^2}{\alpha \rho_l} + \frac{(1-x)^2}{(1-\alpha) \rho_l} \right)_{exit} - \left(\frac{x^2}{\alpha \rho_l} + \frac{(1-x)^2}{(1-\alpha) \rho_l} \right)_{entrance} \right] \quad (45)$$

The two-phase pressure drop in the above equation has two components: frictional and deceleration/acceleration pressure drop. The frictional component can be calculated using the Lockhart-Martinelli (1949) correlation:

$$\Phi^2 = 1 + CX + X^2 \quad (46)$$

$$X^2 = \frac{f_l (1-x)^2 \rho_v}{f_v x^2 \rho_l} \quad (47)$$

Φ^2 = Two-phase pressure drop multiplier.

x = Refrigerant quality.

C = Constant that depends on the respective flow regime for the liquid and vapor phases.

G_t = Mass flux.

L_t = Tube length.

The term in brackets in equation (45) represents the pressure rise or drop due to the deceleration/acceleration of the fluid as it condenses/evaporates. The void fraction α required for this calculation is calculated from the Butterworth (1975) correlation:

$$\alpha = \left[1 + 0.28 \left(\frac{1-x}{x} \right)^{0.64} \left(\frac{\rho_v}{\rho_l} \right)^{0.36} \left(\frac{\mu_l}{\mu_v} \right)^{0.07} \right]^{-1} \quad (48)$$

In practice, the deceleration/acceleration pressure drop term is usually an order of magnitude less than the frictional pressure drop term. For simplicity, this term was not included in the computer program.

Air-side heat transfer and pressure drop

Correlations developed by Sunden and Svantesson (1992) were used to calculate heat transfer and pressure drop through the multilouver fins on the air-side:

$$St_a = j_a Pr_a^{2/3} = 3.67 Re_{Lp}^{-0.591} \left[\frac{f_p}{l_w \cos \theta} \right]^{0.0206} \left[\frac{c_h}{l_w \cos \theta} \right]^{-0.285} \times \left[\frac{l_w \sin \theta}{2l_w \cos \theta} \right]^{0.0671} \left[\frac{c_w}{l_w \cos \theta} \right]^{-0.243} \quad (49)$$

With $h_a = St_a \rho_a V_a c_{p,a}$, the air-side heat transfer coefficient can be calculated. In the above equation, Re_{Lp} is the Reynolds number based on the louver pitch $l_w \cos \theta$, and f_p , c_h , c_w , l_w and θ are fin pitch, center height, center width, louver width and louver angle, respectively.

In cases where moist-air dehumidification occurs, the convection heat transfer coefficient $h_{a,conv}$ was calculated using the dry-surface heat transfer correlation (equation 49) with the dry-surface Reynolds number Re_{Lp} replaced by the wet-surface Reynolds number $Re_{Lp,w}$:

$$Re_{Lp,w} = 4.6 Re_{Lp}^{3/4} \quad (50)$$

This approach is recommended by Kuehn *et al.* (1998). However, $h_{a,conv}$ is the heat transfer coefficient between air and the surface of the water condensate film on the fins. The heat transfer coefficient between air and the fin can be calculated by including the conduction resistance across the liquid film as follows:

$$h_{a,w} = \frac{1}{\frac{c_{p,a}}{b_{w,m} h_{a,conv}} + \frac{t_{water}}{k_{water}}} \quad (51)$$

Where $c_{p,a}$ is the specific heat of air, $b_{w,m}$ is a fictitious moist-air specific heat evaluated at the mean water film temperature $t_{w,m}$, and t_{water} and k_{water} are the thickness and thermal conductivity of the water film, respectively.

The air-side pressure drop can be calculated by the equations developed by Sunden and Svantesson (1992):

$$f_a = 9.2 \text{Re}_{lp}^{-0.540} \left[\frac{f_p}{l_w \cos \theta} \right]^{-0.022} \left[\frac{c_h}{l_w \cos \theta} \right]^{-1.085} \times \left[\frac{l_w \sin \theta}{2l_w \cos \theta} \right]^{0.067} \left[\frac{c_w}{l_w \cos \theta} \right]^{0.310} \quad (52)$$

$$\Delta P_a = \frac{G_a^2}{2 \rho_a D_{h,a}} f_a c_w \quad (53)$$

$$G_a = \frac{\dot{m}_a}{A_{f,a}} \quad (54)$$

Overall heat transfer calculation for dry-surface air-coupled heat exchanger

The overall heat transfer conductance of dry surface is given by:

$$UA = \frac{Q}{F \times LMTD} \quad (55)$$

$$LMTD = \frac{(T_{t,in} - T_{a,out}) - (T_{t,out} - T_{a,in})}{\ln[(T_{t,in} - T_{a,out}) / (T_{t,out} - T_{a,in})]} \quad (56)$$

Where F is the so called F-factor. F-factor is less than unity for a single-phase heat exchanger while the F-factor is equal to unity for phase-change heat transfer. Q is the specified heat duty and can be calculated as follows:

$$Q = \dot{m}_t (h_{t,in} - h_{t,out}) \quad (57)$$

The heat exchanger length can then be calculated using the following equation:

$$L_t = UA \left[\frac{1}{h_t A_{eff,t} N_t} + \frac{t_t}{k_t A_{bt} N_t} + R_c + \frac{1}{h_a A_{eff,a} N_c} \right] \quad (58)$$

Overall heat transfer calculation for wet surface air coupled heat exchanger

In case the fins are wetted by moisture condensed from the air passing over the outside surface, the heat transfer is governed by

$$Q = (UA)_h \Delta h_m \quad (59)$$

where

$$\Delta h_m = \frac{(h_1 - h_{s,R,2}) - (h_2 - h_{s,R,1})}{\ln[(h_1 - h_{s,R,2})/(h_2 - h_{s,R,1})]} \quad (60)$$

h_1 , h_2 are true enthalpies of the entering and leaving air stream, respectively, and $h_{s,R,1}$, $h_{s,R,2}$ are fictitious enthalpies of saturated air calculated at the entering and leaving refrigerant (or other fluid) temperatures. It should be noted that in equation (59), the unit of $(UA)_h$ is different from the UA in equation (55). The unit of $(UA)_h$ is kg/s. Equation (60) is only valid for cases where the refrigerant (or other fluid) temperature change is small. Q is specified heat duty and can be calculated as follows

$$Q = \dot{m}_t (h_{t,in} - h_{t,out}) \quad (61)$$

The heat exchanger length can then be calculated using the following equation:

$$L_t = (UA)_h \left[\frac{b'_R}{h_t A_{eff,t} N_t} + \frac{b_{w,m} t_t}{k_t A_{bt} N_t} + R_c + \frac{b_{w,m}}{h_a A_{eff,a} N_c} \right] \quad (62)$$

Where

$$b'_R = \frac{h_{s,P} - h_{s,R}}{T_P - T_R} \quad (63)$$

$$b_{w,m} = \frac{h_{w,m,1} - h_{w,m,2}}{T_{w,m,1} - T_{w,m,2}} \quad (64)$$

$$T_{w,m,1} = T_{w,m} + 0.5, \quad T_{w,m,2} = T_{w,m} - 0.5 \quad (65)$$

$b'_R, b_{w,m}$ are coefficients evaluated at refrigerant (or other fluid) temperature T_R and mean water-film temperature $T_{w,m}$. These coefficients have the units of specific heat. $h_{s,p}, h_{s,R}$ are the fictitious enthalpies of saturated moist air evaluate at the temperature of the inner tube wall T_p and refrigerant (or other fluid) T_R , respectively. $h_{w,m,1}, h_{w,m,2}$ are the fictitious enthalpies of saturated moist air evaluated at the water-film temperature $T_{w,m,1}$ and $T_{w,m,2}$, respectively.

Overall heat transfer calculation for hydronically coupled heat exchanger

The overall heat transfer calculation is similar to that of a dry-surface air coupled heat exchanger. The *LMTD* can be computed as previously defined. The heat exchanger length can be calculated as:

$$L_t = UA \left[\frac{1}{h_r A_{eff,r} N_{t,r}} + \frac{t_{t,r}}{k_{t,r} A_{bt,r} N_{t,r}} + R_c + \frac{t_{t,h}}{k_{t,h} A_{bt,h} N_{t,h}} + \frac{1}{h_h A_{eff,h} N_{t,h}} \right] \quad (66)$$

Results for the Component Designs Using Lumped Heat Exchanger Model

The microchannel heat exchangers in both air-coupled and hydronically coupled systems were optimized to yield the least possible mass while meeting the pressure drop requirements for both fluids. As stated in the previous chapter, these heat exchangers were designed for both the heating and cooling mode conditions, and the larger of the two sizes for each of these heat exchangers was picked for the system. Table 16 gives the optimized heat exchanger size for both air-coupled and hydronically coupled systems. Table 17 and 18 list the optimized heat exchanger geometries.

The state points as well as the system performance computed from the integrated system model with compressor and lumped heat exchangers models were different from the idealized system because of the pressure drop and the corresponding saturation temperature change in the lumped heat exchanger models. Tables 19 to 22 list the new state points and the system performance of integrated systems for air-coupled and hydronically coupled systems, respectively. In these tables, the state point numbers [1], [3], [4] and [8] refer to the

Table 16. Optimized Heat Exchanger Sizes

	Air Coupled System		Hydronically Coupled System			
	Indoor Unit	Outdoor Unit	Condenser	Evaporator	Indoor Unit	Outdoor Unit
Length (m)	0.568	0.652	0.954	0.680	0.848	1.046
Height (m)	0.336	0.530	0.026	0.043	0.475	0.950
Depth (m)	0.040	0.045	0.090	0.090	0.040	0.040
Mass (kg)	4.39	7.18	2.54	2.92	10.05	20.88
Heat Duty (KW)	10.6 (s) 15.0 (w)	12.4 (s) 11.7 (w)	12.4 (s) 15.0 (w)	10.5 (s) 12.1 (w)	10.6(s) 15.0 (w)	15.1 (s) 12.1 (w)

Note s: Summer mode, w: Winter mode

Table 17. Geometric Features of the Optimized Air-Coupled Heat Exchangers

	Air Coupled System		Hydronically Coupled System	
	Indoor Unit	Outdoor Unit	Indoor Unit	Outdoor Unit
Outside tube height (m)	0.0015	0.0013	0.0022	0.0055
Outside tube width (m)	0.040	0.045	0.040	0.040
Tube wall thickness (m)	0.318e-3	0.318e-3	0.318e-3	0.318e-3
Number of webs	19	19	10	17
Web thickness (m)	0.318e-3	0.318e-3	0.318e-3	0.318e-3
Number of tubes per pass	14	17	19	20
Tube wall roughness	0	0	0	0
Number of centers per pass	14	17	19	20
Center (fin) height (m)	0.0045	0.0065	0.0028	0.0040
Center depth (m)	0.04	0.045	0.04	0.04
Fin thickness (m)	0.127e-3	0.127e-3	0.127e-3	0.127e-3
Fin pitch (m)	0.0016	0.0018	0.0016	0.0017
Number of passes	4	4	5	5
Louver width (m)	0.001	0.001	0.001	0.001
Louver length (m)	0.9c _h	0.9c _h	0.9c _h	0.9c _h
Louver angle (°)	30	30	30	30

Table 18. Geometric Features of the Optimized Hydronically Coupled Heat Exchangers

	Condenser		Evaporator	
	Refrigerant Side	Glycol Water Side	Refrigerant Side	Glycol Water Side
Outside tube height	0.0010	0.0020	0.0010	0.0027
Outside tube width	0.09	0.09	0.09	0.09
Tube wall thickness	0.2e-3	0.2e-3	0.2e-3	0.2e-3
Number of webs	108	92	110	110
Web thickness	0.2e-3	0.2e-3	0.2e-3	0.2e-3
Number of tubes per pass	8	9	11	12
Tube wall roughness	0	0	0	0

Table 19. State Points of Air-Coupled System Designed for Heating Mode

State Point Number.	Cooling Mode			Heating Mode		
	Temperature (°C)	Pressure (kPa)	Enthalpy (kJ/kg)	Temperature (°C)	Pressure (kPa)	Enthalpy (kJ/kg)
1	11.62	714.03	94.50	-0.09	495.84	92.04
3	18.96	686.48	260.12	-2.72	454.59	248.94
4	73.81	1704.87	289.06	89.11	1769.19	301.62
8	40.09	1685.58	94.50	38.13	1753.25	92.04
9	27.00	101.33	56.24	8.30	101.33	20.74
10	14.20			3.02		
11	35.00	101.33	91.65	21.10	101.33	44.09
12	41.81			43.00		

Table 20. Performance of Air-Coupled System Designed for Heating Mode

	Cooling Mode	Heating Mode
$Q_{\text{evaporator}}$ (KW)	10.55	11.70
$Q_{\text{condenser}}$ (KW)	12.39	15.00
$\text{COP}_{\text{cooling}}$	3.72	
$\text{COP}_{\text{heating}}$		2.95
Compressor Power (KW)	2.84	5.08
Delivered Temperature (°C)	14.20	43.00
Refrigerant Flow Rate (kg/s)	0.06370	0.07159
Refrigerant Charge (kg)	1.520	1.681

Table 21. State Points of Hydronically Coupled System Designed for Heating Mode

State Point Number.	Cooling Mode			Heating Mode		
	Temperature (°C)	Pressure (kPa)	Enthalpy (kJ/kg)	Temperature (°C)	Pressure (kPa)	Enthalpy (kJ/kg)
1	9.83	676.67	99.47	-3.07	449.36	93.00
3	13.78	657.30	256.77	4.97	422.12	255.06
4	75.34	1829.15	288.73	93.64	1844.70	304.69
8	43.81	1809.49	99.47	38.82	1827.11	93.00
9	16.52			5.00		
10	10.59			-1.55		
11	39.23			37.65		
12	46.20			45.92		
13	27.00	101.33	56.25	8.30	101.33	20.74
14	14.31			3.01		
15	35.00	101.33	91.65	21.10	101.33	44.09
16	43.48			43.00		

Table 22. Performance of Hydronically Coupled System Designed for Heating Mode

	Cooling Mode	Heating Mode
$Q_{evaporator}$ (KW)	10.55	11.51
$Q_{condenser}$ (KW)	12.67	15.03
Q_{cold} (KW)	10.53	11.62
Q_{hot} (KW)	15.35	15.00
$COP_{cooling}$	3.21	
$COP_{heating}$		2.76
Compressor Power (KW)	3.29	5.42
Delivered Temperature (°C)	14.31	43.00
Refrigerant Flow Rate (kg/s)	0.06693	0.07101
Refrigerant Charge (kg)	0.195	0.187

refrigerant state at evaporator inlet, evaporator superheated outlet, condenser inlet and condenser subcooled outlet, respectively. State points [9] to [12] refer to evaporator air/hydronic fluid inlet, evaporator air/hydronic fluid outlet, condenser air/hydronic fluid inlet and condenser air/hydronic fluid outlet, respectively. State points [13] to [16] refer to the cold side air-to-hydronic fluid heat exchanger inlet and outlet, and hot side air-to-hydronic fluid heat exchanger inlet and outlet, respectively.

CHAPTER 4. COMPRESSOR MODELING

The compressor model employed here is a loss and efficiency-based model from the Oak Ridge Heat Pump Models (Fischer and Rice, 1983). It is based on the internal energy balances in a reciprocating compressor from the specified internal efficiency and heat loss values. The sketch below shows the compressor's energy balance (Figure 21). This figure shows the following energy streams:

Q_{can} = Compressor shell heat loss, specified,

$Q_{cooling}$ = Heat loss due to cooling of compressor and motor, specified,

Q_{hilo} = Compressor heat transfer rate from discharge gas to suction gas, specified,

W_{cm} = Compressor input power,

W_r = Work done on the refrigerant.

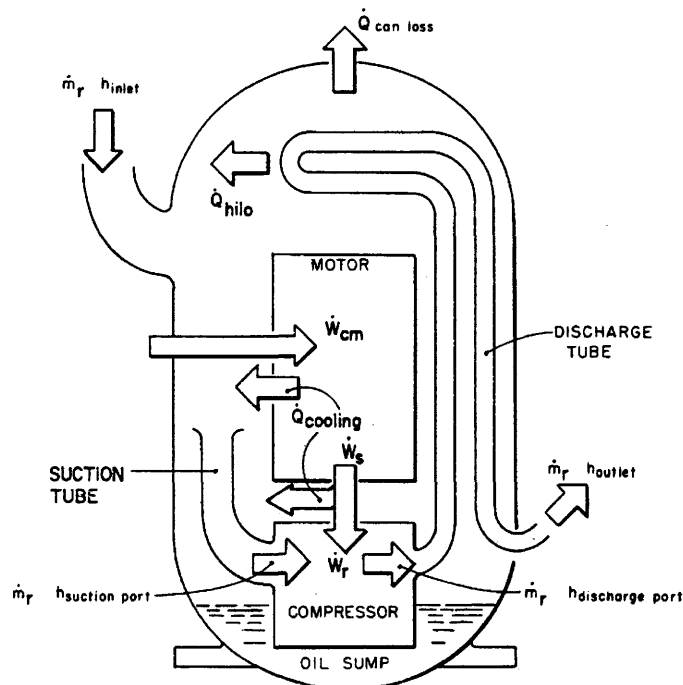


Figure 21. Energy Balance for the Compressor (Fischer and Rice, 1983)

The design conditions and other specified properties for the compressor model are listed in Table 23.

The modeling procedure for the compressor is shown in Figure 22.

The refrigerant state at the suction and discharge ports can be calculated using the equations below:

$$P_{suction} = P_{inlet} - \Delta P_{suction} \quad (67)$$

$$P_{discharge} = P_{outlet} + \Delta P_{discharge} \quad (68)$$

The work done on the refrigerant, shaft power and compressor power input can be solved by the following equations:

$$W_r = m_r (h_{discharge} - h_{suction}) \quad (69)$$

Table 23. Input Variables for the Compressor Model

Symbols	Input Variables
C	Compressor actual clearance volume ratio, 0.06
n	Refrigerant polytropic exponent, 1.07
η_{motor}	Compressor motor efficiency, 0.82
η_{mech}	Compressor mechanical efficiency, 0.8
η_{isen}	Compressor isentropic efficiency, 0.7
$\Delta P_{suction}$	Pressure difference between compressor inlet and suction port, 12Kpa
$\Delta P_{discharge}$	Pressure difference between compressor outlet and discharge port, 24Kpa
Q_{can}	$Q_{can} = 0.35W_{cm}$
Q_{hilo}	$Q_{hilo} = 0.03W_{cm}$
$Q_{cooling}$	$Q_{cooling} = (1 - \eta_{mech}\eta_{motor})W_{cm}$
m_r	Refrigerant mass flow rate
h_{inlet}	Refrigerant enthalpy at compressor inlet
P_{inlet}	Refrigerant pressure at compressor inlet
T_{inlet}	Refrigerant at temperature compressor inlet
P_{outlet}	Refrigerant pressure at compressor outlet

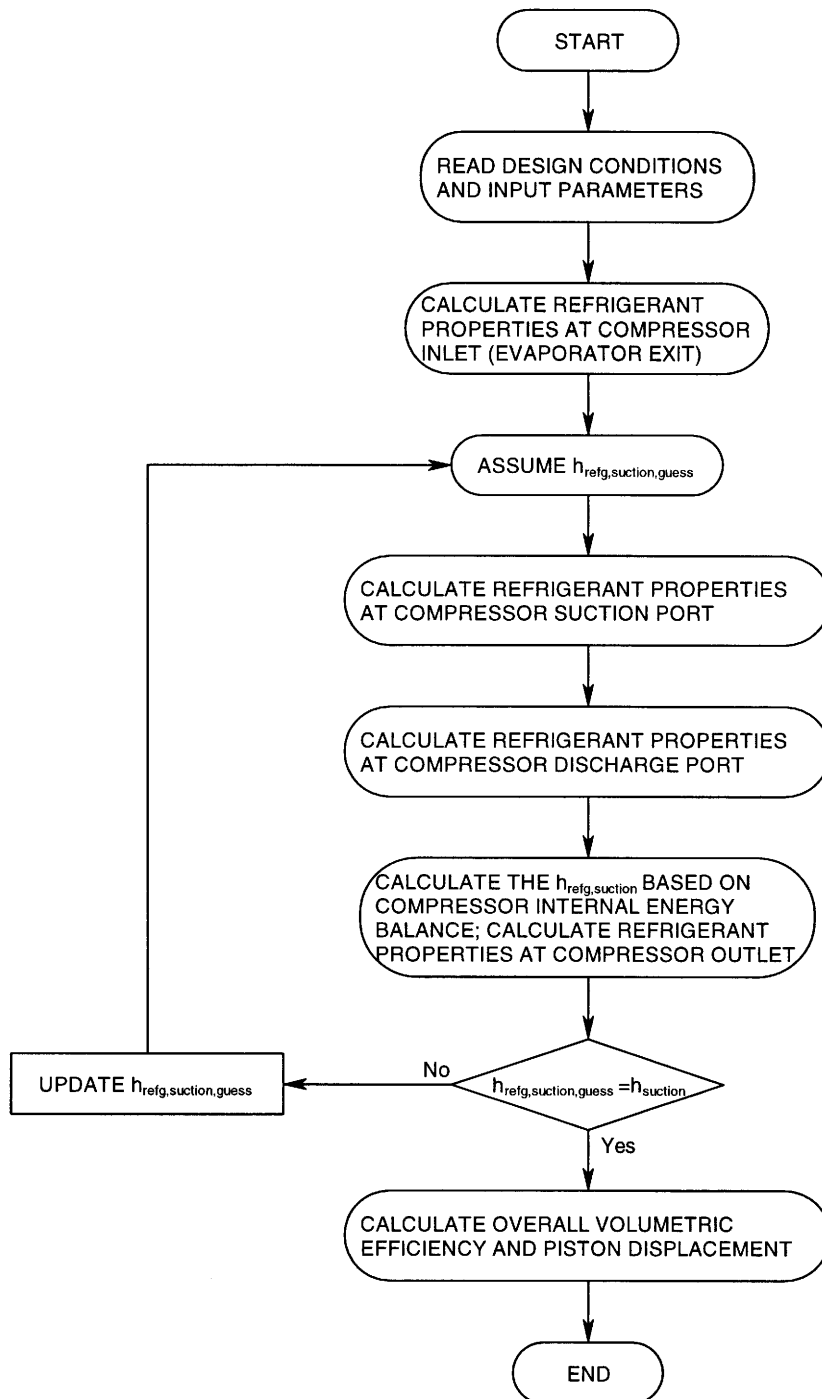


Figure 22. Compressor Modeling Procedure

$$W_s = \frac{W_r}{\eta_{mech}} \quad (70)$$

$$W_{cm} = \frac{W_s}{\eta_{motor}} \quad (71)$$

In this compressor model, compression between the suction port and the discharge port was computed using the supplied isentropic efficiency. Therefore:

$$s_{isen, discharge} = s_{suction} \quad (72)$$

$$\eta_{isen} = \frac{h_{isen, discharge} - h_{suction}}{h_{discharge} - h_{suction}} \quad (73)$$

$$h_{isen, discharge} = f_1(s_{isen, discharge}, P_{discharge}) \quad (74)$$

$$T_{discharge} = f_2(h_{discharge}, P_{discharge}) \quad (75)$$

The assumed refrigerant enthalpy at the compressor suction port can be corrected based on the compressor internal energy balance represented by the following equations:

$$m_r(h_{suction} - h_{inlet}) = Q_{hilo} + Q_{cooling} - Q_{can} \quad (76)$$

$$m_r(h_{outlet} - h_{discharge}) = -Q_{hilo} \quad (77)$$

$$T_{outlet} = f(h_{outlet}, P_{outlet}) \quad (78)$$

The compressor volumetric efficiency and piston displacement can be determined as follows:

$$\eta_{v,theory} = \left[1 + C - C \left(\frac{P_{discharge}}{P_{suction}} \right) \right]^{1/n} \left(\frac{v_{inlet}}{v_{suction}} \right) \quad (79)$$

$$\eta_v = \eta_{v,theory} - a \left(\frac{\gamma - 1}{\gamma} \times \frac{P_{discharge}}{P_{suction}} \right) - b \quad (80)$$

$$PD = \frac{m_r v_{inlet}}{\eta_v} \quad (81)$$

Where a and b are empirical constants derived from test data for compressors of different capacities but of the same series (Fischer and Rice, 1983). In the above equations, $a = 0.733$, and $b = -0.0933$.

CHAPTER 5. INCREMENTAL ANALYSIS OF TWO-PHASE HEAT TRANSFER

In phase change processes, fluid properties change dramatically as the fluid changes from vapor to liquid or vice versa. Since the change in fluid properties will affect the heat transfer coefficient and pressure drop, the sizes of the two-phase heat exchangers were also computed using an incremental approach. In this approach, each heat exchanger was divided into segments of equal quality change with $\Delta x = 0.05$. Heat transfer coefficient and pressure drop in each segment were calculated based on the properties at the average quality for that segment. This approach provides more accurate results because it addresses the changes in heat transfer coefficient and pressure drop as the fluid undergoes phase change.

Figures 23 and 24 show the temperature profile and required heat exchanger UA for each segment in the air-coupled condenser. As the refrigerant condenses, the required UA decreases slightly because of the increasing temperature difference between the refrigerant and air. As shown in Figure 25, the air-side heat transfer resistance is dominant and remains essentially constant across the heat exchanger. The refrigerant resistance increases toward the exit because of the decreasing refrigerant heat transfer coefficient, which is in turn due to the gravity-dominated flows at low qualities. The net effect is that the total resistance increases toward the exit of the condenser. Figure 26 shows the combined effect of this increasing resistance (Figure 25) and the decreasing UA requirement toward the condenser exit (Figure 24). Thus, the effect of the increasing resistance dominates, and the length required increases at lower qualities. Figure 27 and 28 show the variation of refrigerant and air pressure drop as a function of refrigerant average quality, respectively. As discussed in Chapter 3, the refrigerant pressure drop is proportional to the segment length and is a function of refrigerant quality. Near the inlet and outlet of the condenser, the pressure drop approaches the corresponding single-phase vapor and single-phase liquid values, with the ΔP near the inlet being higher due to the higher gas-phase velocities. At intermediate locations, the pressure drop is higher because of the shear between the two phases (two-phase multiplier). Similarly, the air-side pressure drop is proportional to the square of the air velocity. The air velocity decreases towards the exit of the condenser because of the lower refrigerant and air temperature, which results in a lower air-side pressure drop.

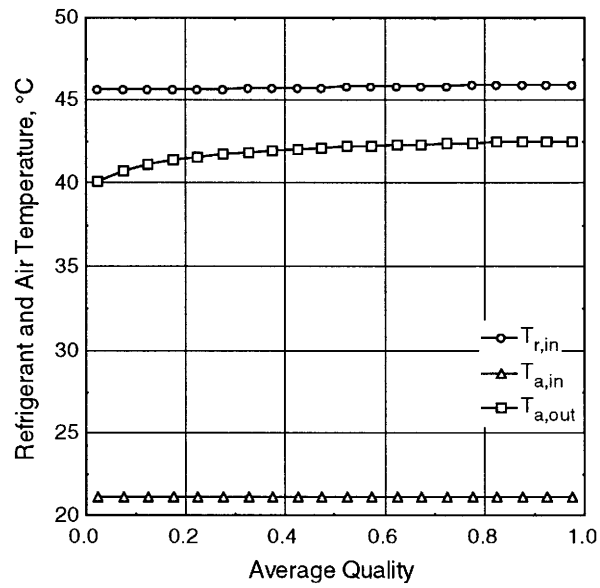


Figure 23. Temperature Profile in the Air-Coupled Condenser

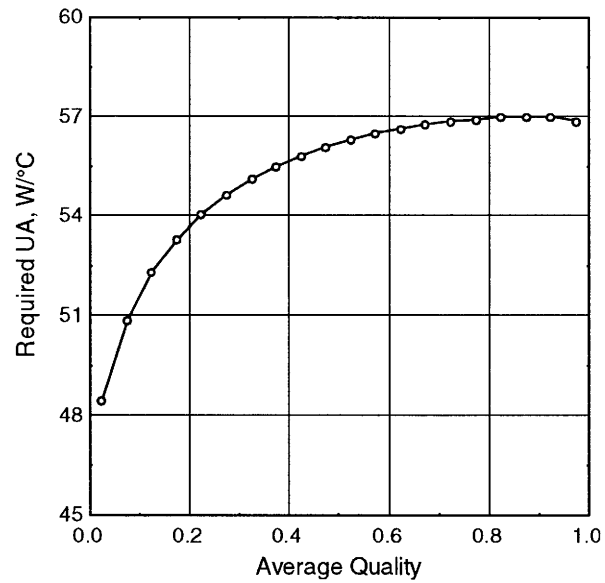


Figure 24. Required UA Per Segment in the Air-Coupled Condenser

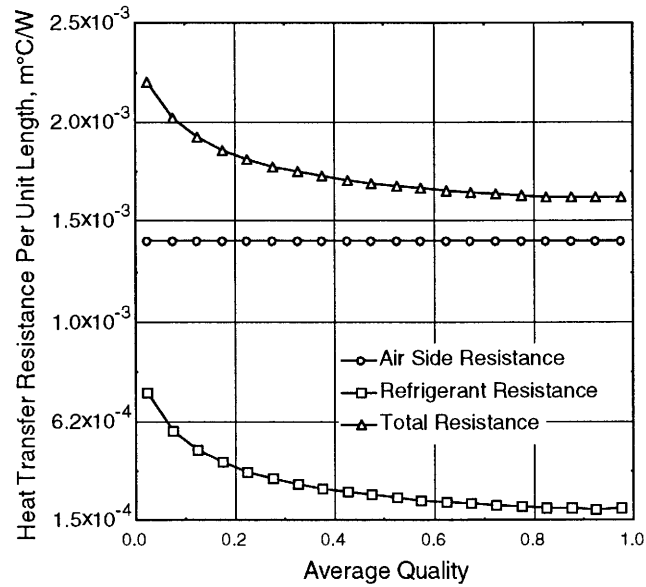


Figure 25. Heat Transfer Resistances in the Air-Coupled Condenser

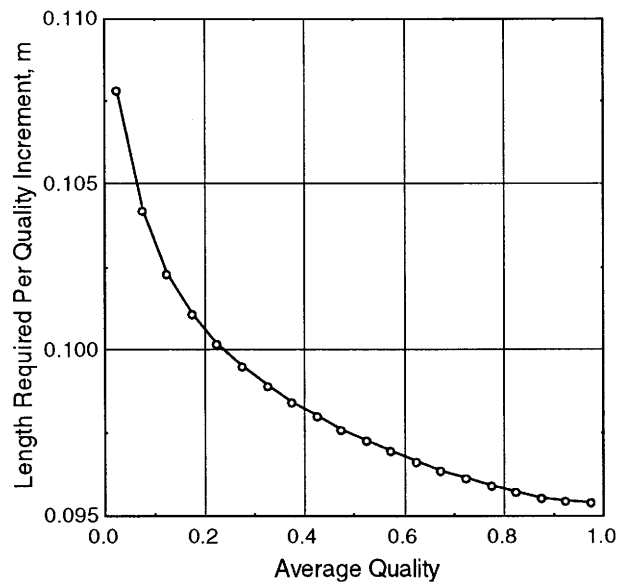


Figure 26. Length Required Per Quality Increment in the Air-Coupled Condenser

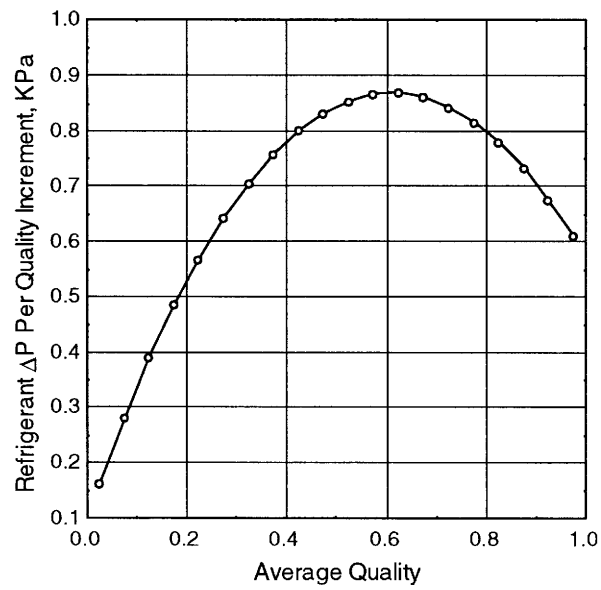


Figure 27. Refrigerant Pressure Drop Variation with Average Quality (Air-Coupled Condenser)

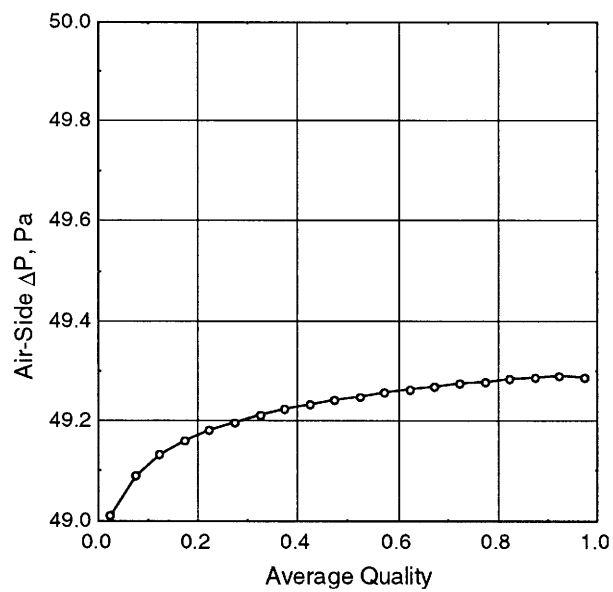


Figure 28. Air-Side Pressure Drop Variation Across the Air-Coupled Condenser

Similar results are shown for the air-coupled evaporator in Figures 29 through 37. These figures are based on results for an evaporator designed for the heating mode. It should be noted that this evaporator is smaller than the design needed for it to operate as an indoor unit in the cooling mode, and therefore does not meet the design requirements. However, this configuration illustrates the approach for the two-phase incremental analysis better because it spans a larger quality range, and a smaller fraction of this component is in the superheated vapor region near the exit.

Figure 29 shows the temperature profile in the air-coupled evaporator for the refrigerant, air and water condensate film. It should be noted that the mean water film temperature, $T_{w,m}$, is below 0°C at $x \approx 0.77$ indicating that frosting could occur. Figure 30 shows the discontinuity in water conductivity in this region because of this phase-change process. As discussed in Chapter 3, the wet-surface heat transfer coefficient between air and the fin surface is a function of water film thickness t_{water} , water conductivity k_{water} , coefficient $b_{m,w}$, and the convective heat transfer coefficient between air and the water-film

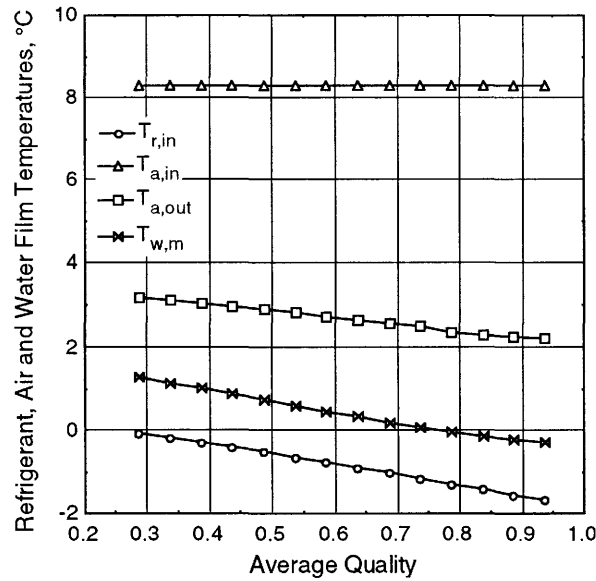


Figure 29. Temperature Profile in the Air-Coupled Evaporator

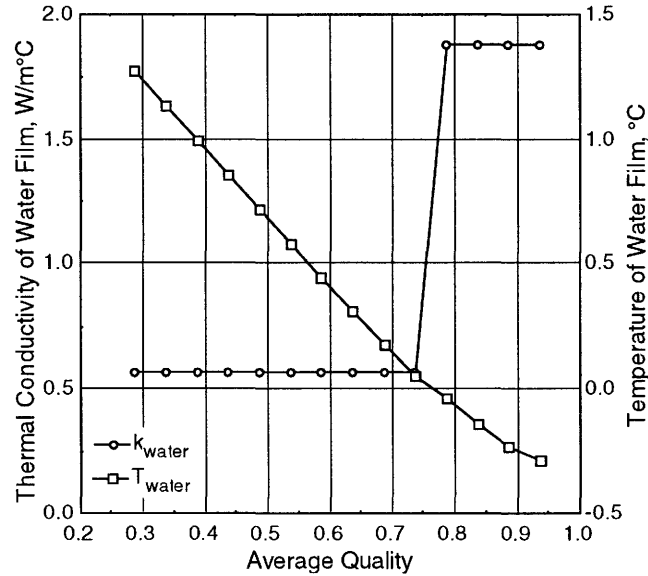


Figure 30. Thermal Conductivity of Water Film on the Fins

surface $h_{a,conv}$. Figures 31 and 32 show the coefficient $b_{m,w}$ and convective heat transfer coefficient $h_{a,conv}$ as a function of refrigerant average quality across the evaporator, respectively. The slope change at the 10th data point ($x \approx 0.77$ in Figure 32) reflects the frosting process, which will result in a lower air temperature. Figure 33 shows the resulting air-side wet-surface heat transfer coefficient $h_{a,w}$ as a function of refrigerant average quality, which reflects these variations. Since $h_{a,w}$ is proportional to k_{water} and $b_{m,w}$, the net effect of the variations in k_{water} , $b_{m,w}$ and $h_{a,conv}$ is seen in the slope changes in the wet-surface heat transfer coefficient across the evaporator. The air-side wet-surface heat transfer coefficient decreases much faster than the corresponding convective heat transfer coefficient because of the decrease in k_{water} and $b_{m,w}$ for the first 6 data points. At $x \approx 0.54$, although k_{water} still decreases slightly, the dramatic increase in $b_{m,w}$ results in the increase in $h_{a,w}$. At the 10th data point ($x \approx 0.77$ in Figure 32), frosting starts to occur and k_{water} jumps to the much higher conductivity of ice, resulting in the corresponding increase in the wet-surface heat transfer coefficient. However, it should be noted that the absolute value of these changes is

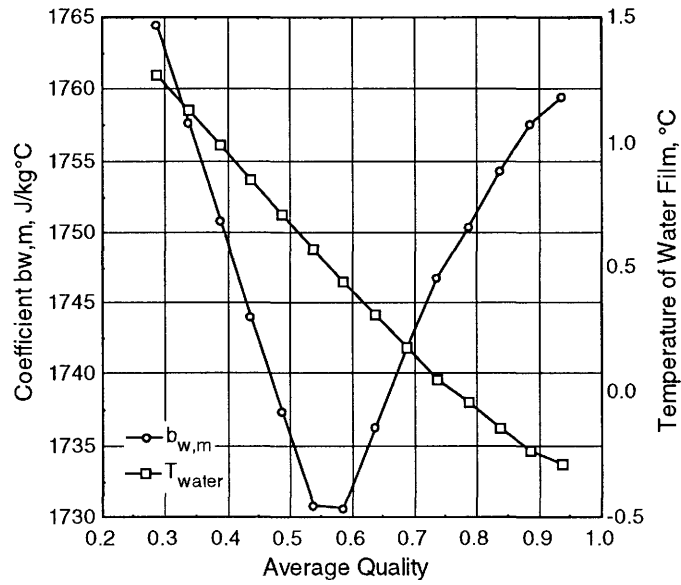


Figure 31. Coefficient $b_{m,w}$ as a Function of Refrigerant Average Quality

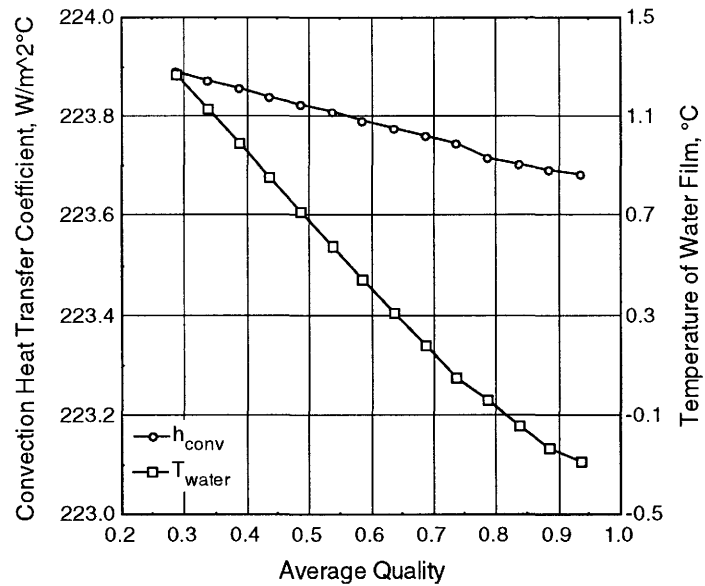


Figure 32. Convective Heat Transfer Coefficient between Air and Water Film Surface

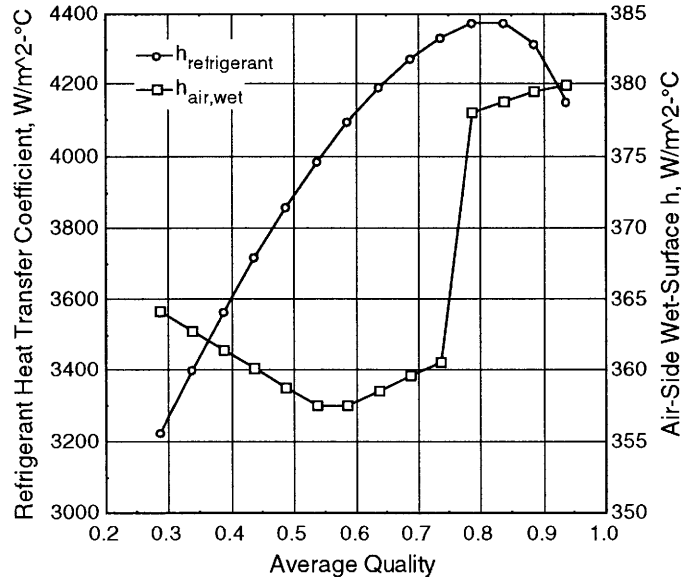


Figure 33. Heat Transfer Coefficient Variation in the Air-Coupled Evaporator

relatively insignificant.

As shown in Figure 34, the required UA decreases towards the exit of the evaporator because of the increasing temperature difference between the refrigerant and air (Figure 29). It should be noted that the unit of the UA is kg/s. This is because the logarithmic enthalpy method is used instead of logarithmic temperature to compute heat transfer in the air-coupled evaporator. The refrigerant heat transfer coefficient increases through most of the evaporator except near the exit where it is governed by the vapor-phase properties (Figure 33), while the required UA per segment decreases (Figure 34). Thus, the length required for each segment decreases at higher qualities (Figure 35). The dryout condition was investigated and the results are shown in Figure 36. According to Levitan and Lantsman (1975), the dryout quality for an 8 mm tube can be predicted by the following equation:

$$x_{crit,8mm} = \left[0.39 + 1.57 \left(\frac{P_{sat}}{98} \right) - 2.04 \left(\frac{P_{sat}}{98} \right)^2 + 0.68 \left(\frac{P_{sat}}{98} \right)^3 \right] \left(\frac{G}{1000} \right)^{-0.5} \quad (82)$$

Where P_{sat} is the refrigerant saturation pressure in bar, and G is the refrigerant mass flux in kg/m²s. For other tube diameters, the USSR Academy of Sciences (1976) recommended the

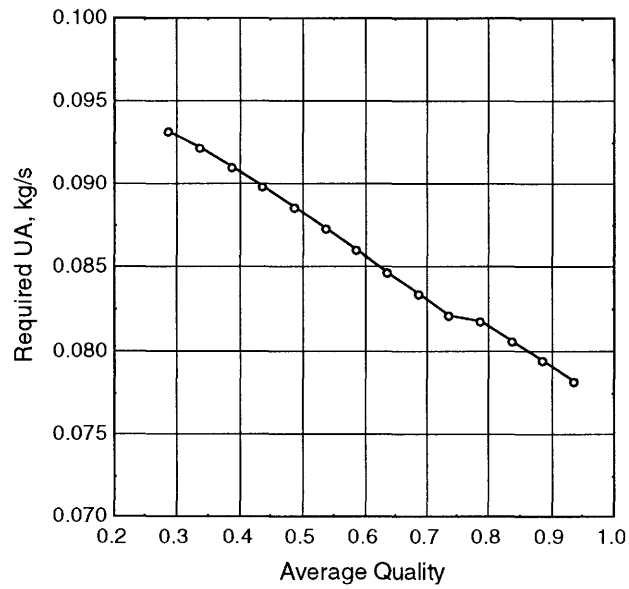


Figure 34. Required UA in the Air-Coupled Evaporator

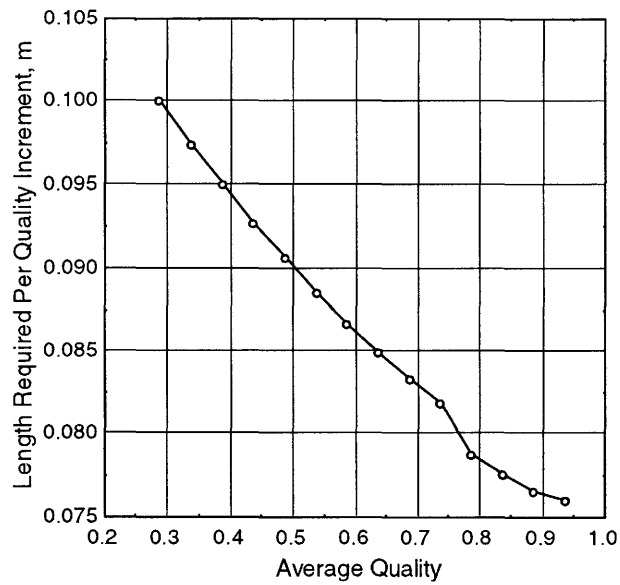


Figure 35. Length Required Per Quality Increment in the Air-Coupled Evaporator

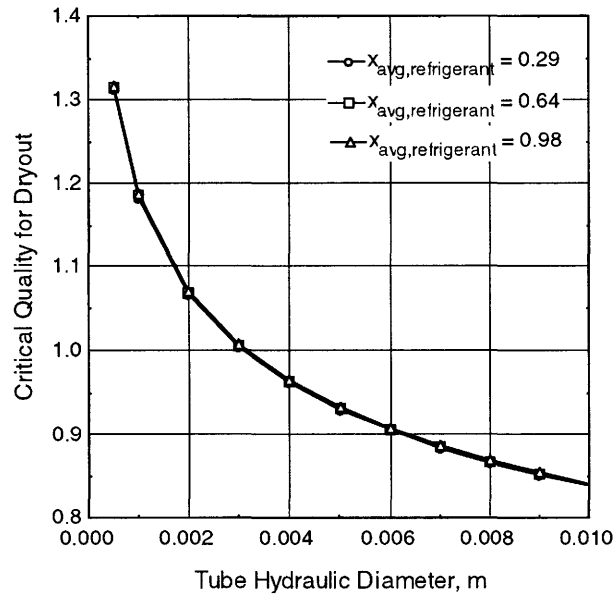


Figure 36. Critical Refrigerant Quality as a Function of Tube Diameter

following equation:

$$x_{crit} = x_{crit, 8mm} \left(\frac{8}{D} \right)^{-0.5} \quad (83)$$

Where D is in millimeters. The dryout condition is investigated at three locations in the evaporator: entrance ($x_{avg} = 0.29$), $x_{avg} = 0.64$ and exit ($x_{avg} = 0.98$). From Figure 36, it can be seen that dryout can only occur for tube diameters larger than 0.0025 m. Therefore, it is expected that for the present case ($D = 0.000988$ m), dryout will not occur because of the extremely small hydraulic diameter.

Figures 37 and 38 show the pressure drop variation of the refrigerant and air as a function of refrigerant average quality, respectively. In Figure 37, the refrigerant pressure drop first increases and then decreases towards the exit of the evaporator. Again, this is because of the progression from low quality to high quality and the associated high vapor velocities, and then the approach to single-phase gas pressure drop. The effect of frosting can also be seen in Figures 34 to 37. The air-side pressure drop decreases slightly towards the exit of the evaporator (Figure 38). This is because of the cooler air temperature and the correspondingly lower air velocities at the higher densities near the evaporator exit.

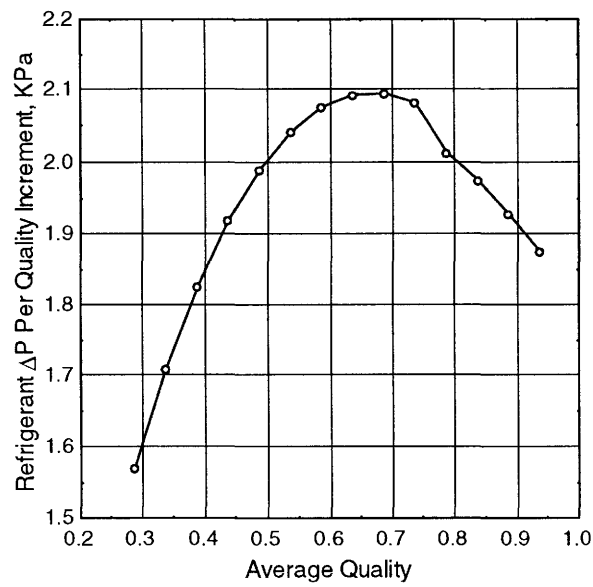


Figure 37. Refrigerant Pressure Drop Variation in the Air-Coupled Evaporator

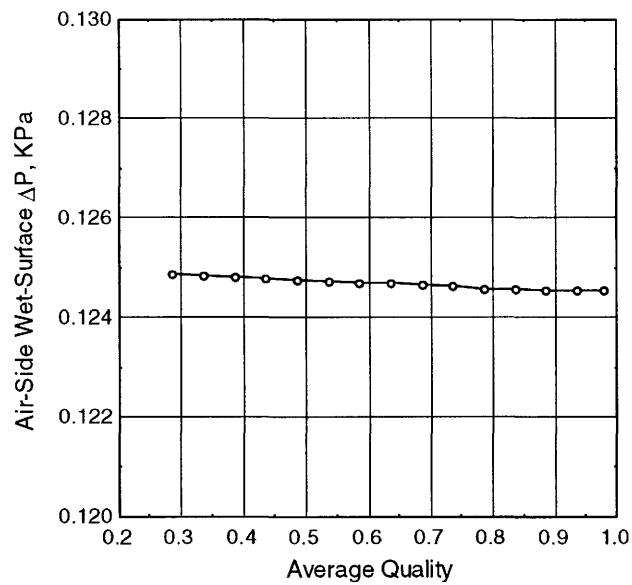


Figure 38. Air Side Wet-Surface Pressure Drop in the Air-Coupled Evaporator

In the hydronically coupled heat exchanger, the two fluids flow countercurrent to each other. Figures 39 through 51 show the results of the incremental analysis of the hydronically coupled condenser and evaporator.

Figures 39 and 40 show that, at low quality, the required UA is small because of the large ΔT between the refrigerant and hydronic fluid. Figure 41 shows that the heat transfer resistance of the hydronic fluid is almost constant throughout the condenser, as expected for this single-phase coolant. Refrigerant heat transfer resistance per unit tube length decreases as the quality increases. This is because the refrigerant heat transfer coefficient decreases towards the low quality region near the exit of the condenser. Thus, the total heat transfer resistance per unit tube length increases at lower qualities. The variations in the required UA and the heat transfer resistance result in the variation in the length required per quality increment show in Figure 42, which shows a minima near $x \cong 0.3$. Refrigerant pressure drop decreases as it condenses (Figure 43) as explained in the discussion of the air-coupled condenser. Since single-phase pressure drop is proportional to the length, the pressure drop in the hydronic fluid follows the trend exhibited by the segment length (Figure 44).

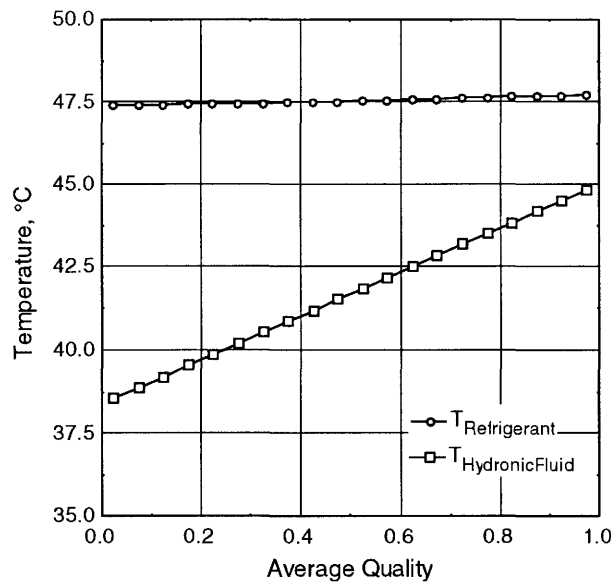


Figure 39. Temperature Profile in the Hydronically Coupled Condenser

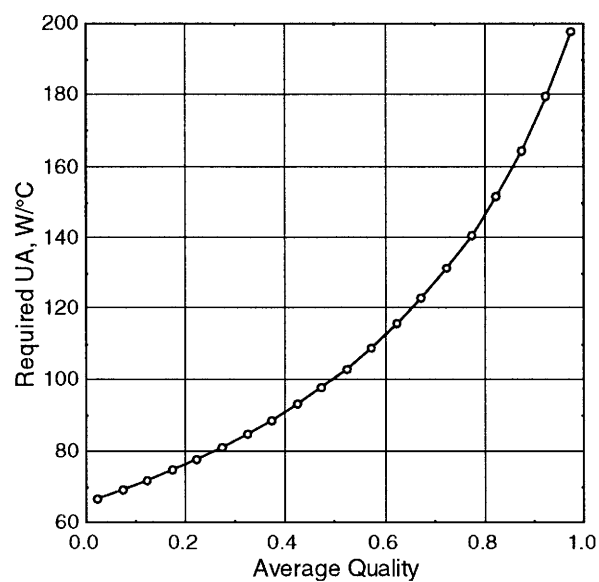


Figure 40. Required Heat Exchanger UA in the Hydronically Coupled Condenser

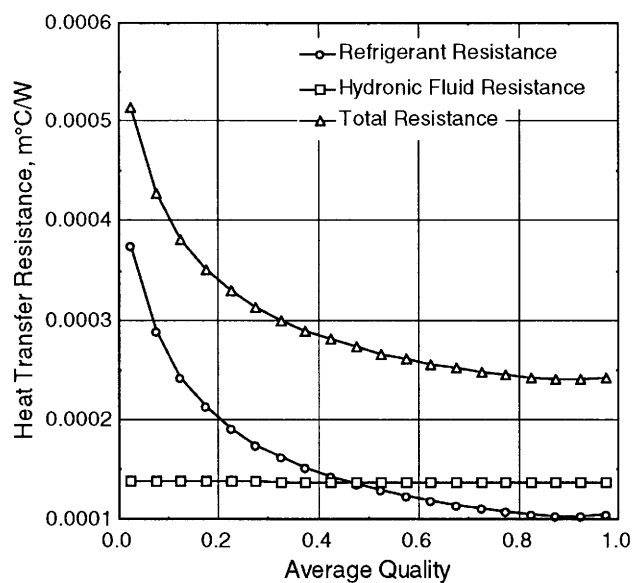


Figure 41. Heat Transfer Resistances in the Hydronically Coupled Condenser

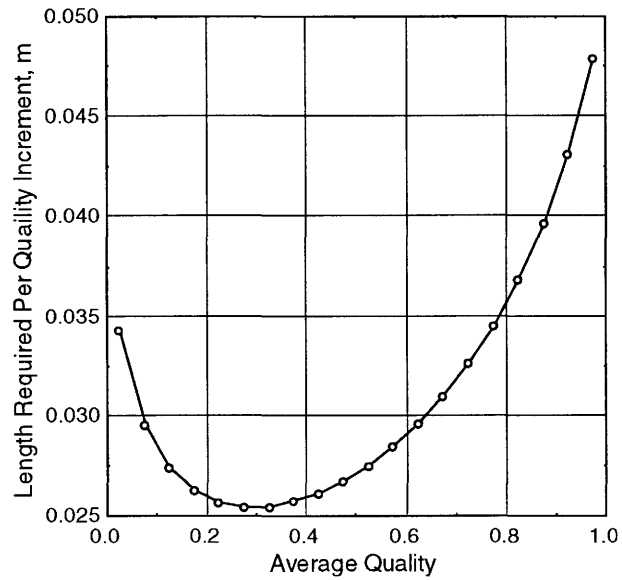


Figure 42. Length Required Per Quality Increment in the Hydronically Coupled Condenser

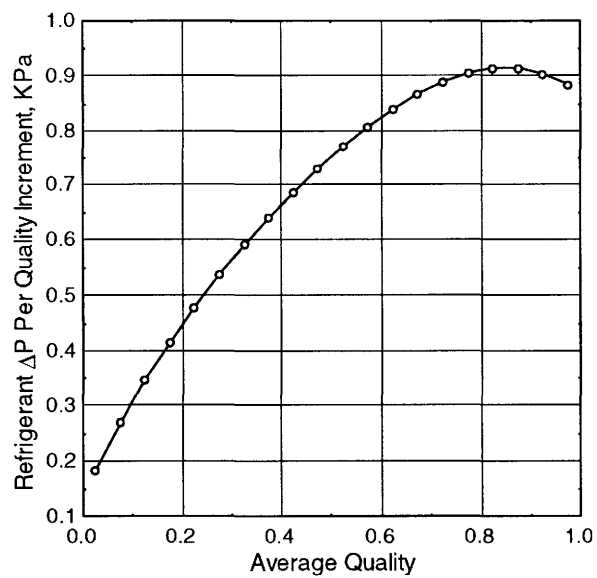


Figure 43. Refrigerant Pressure Drop Per Quality Increment (Hydronically Coupled Condenser)

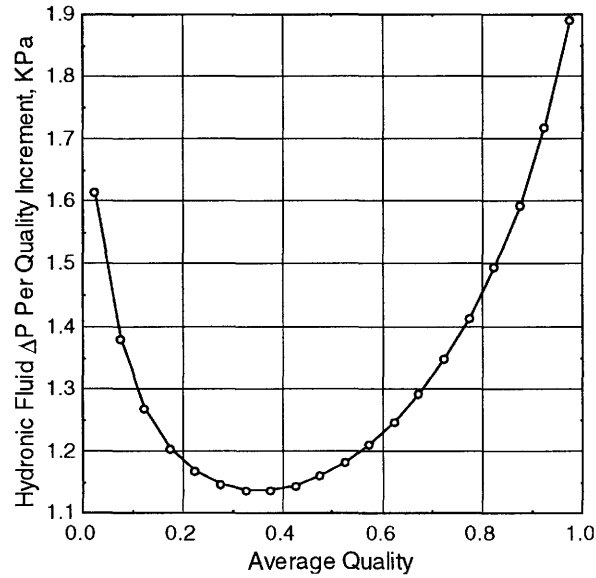


Figure 44. Hydronic Fluid Pressure Drop Per Quality Increment
(Hydronically Coupled Condenser)

Similarly, in the hydronically coupled evaporator, the refrigerant-to-hydraulic fluid temperature difference increases as the quality increases (Figure 45), which leads to the decrease in the required UA (Figure 46). Although the total heat transfer resistance increases in the high quality region near the exit (Figure 47), the length required per quality increment still decreases as the refrigerant evaporates due to the lower UA required (Figure 48). It should be noted that in Figure 47, the hydronic fluid side single-phase heat transfer resistance is lower than the refrigerant evaporation resistance. This is because the effective heat transfer area on the hydronic fluid side is much larger than on the refrigerant side. That is, for a unit tube length (1 m), the hydronic fluid-side effective heat transfer area is $A_{eff,h} = 0.68 \text{ m}^2$, while the refrigerant-side effective heat transfer area is $A_{eff,r} = 0.28 \text{ m}^2$. The corresponding heat transfer coefficients are $h_{hyd} = 2014 \sim 2043 \text{ W/m}^2\text{ }^\circ\text{C}$ on the hydronic fluid side and $h_{refg} = 2773 \sim 4017 \text{ W/m}^2\text{ }^\circ\text{C}$ on the refrigerant-side.

Figure 49 shows the critical refrigerant quality for dryout in the hydronically coupled evaporator, predicted using equations (82) and (83). The dryout condition is again investigated at three locations in the evaporator: entrance ($x_{avg} = 0.31$), $x_{avg} = 0.66$ and exit

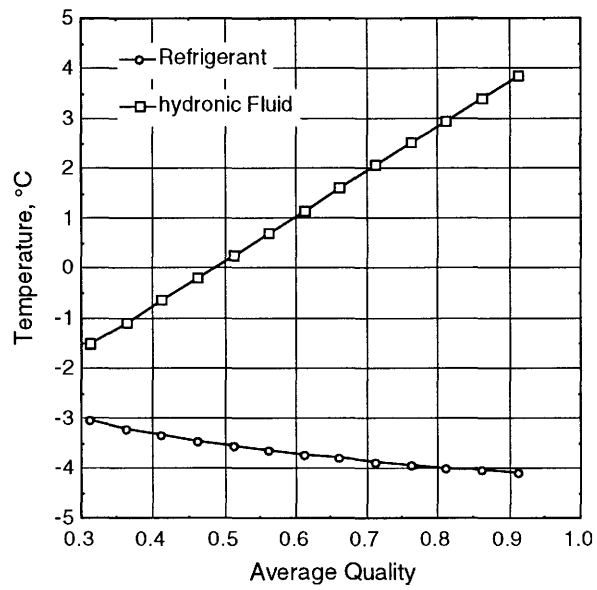


Figure 45. Temperature Profile in Hydronically Coupled Evaporator

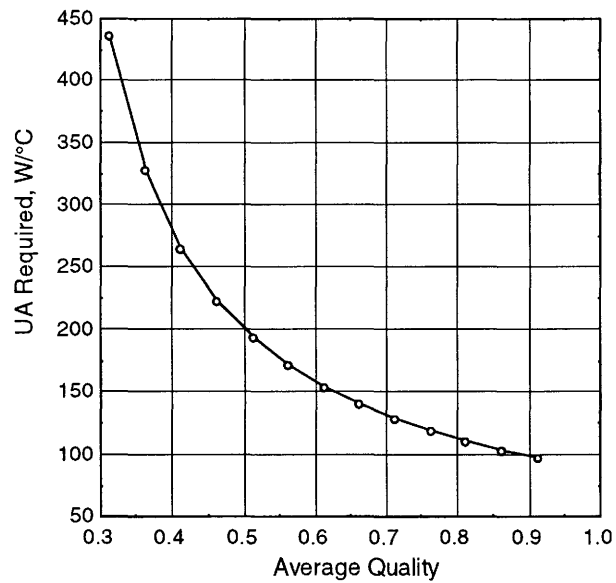


Figure 46. Required Heat Exchanger UA Per Quality Increment (Hydronically Coupled Evaporator)

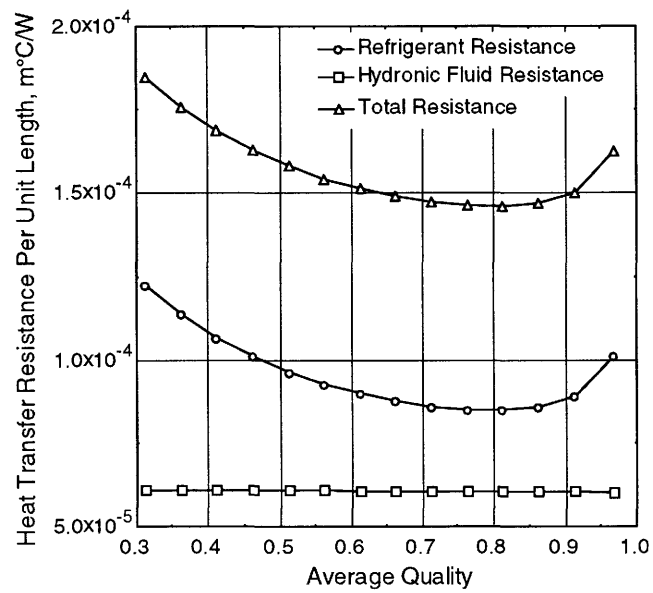


Figure 47. Heat Transfer Resistance Variation with Average Quality (Hydronically Coupled Evaporator)

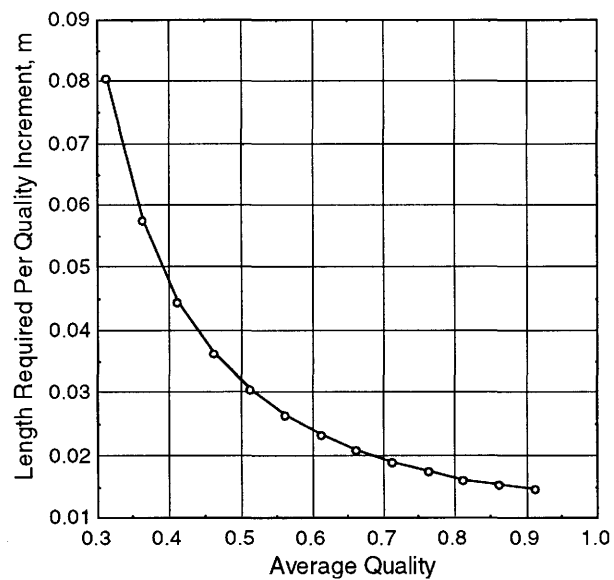


Figure 48. Length Required As a Function of Average Quality (Hydronically Coupled Evaporator)

($x_{avg} = 0.97$). Once again, Figure 49 shows that dryout only occurs for tube diameters larger than 0.004 m. In the present case, $D = 0.000605$ m, indicating that dryout will not occur.

Figures 50 and 51 show that the pressure drop per quality increment of both fluids decreases as the quality increases, which is primarily due to the decrease in length requirement.

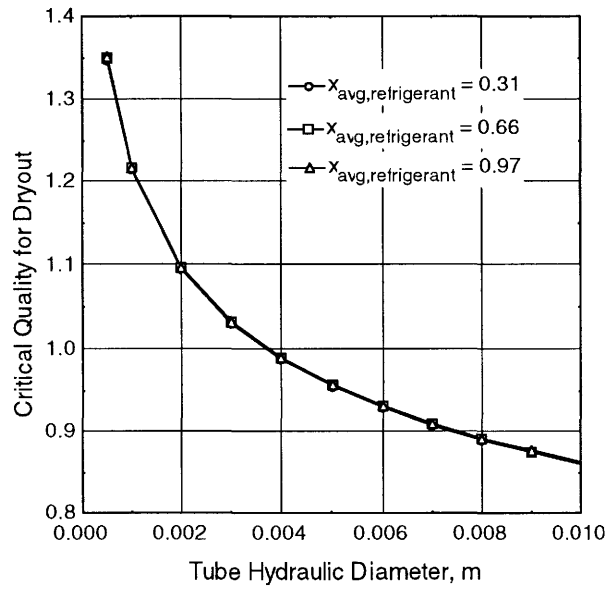


Figure 49. Critical Refrigerant Quality for Dryout as a Function of Tube Diameter

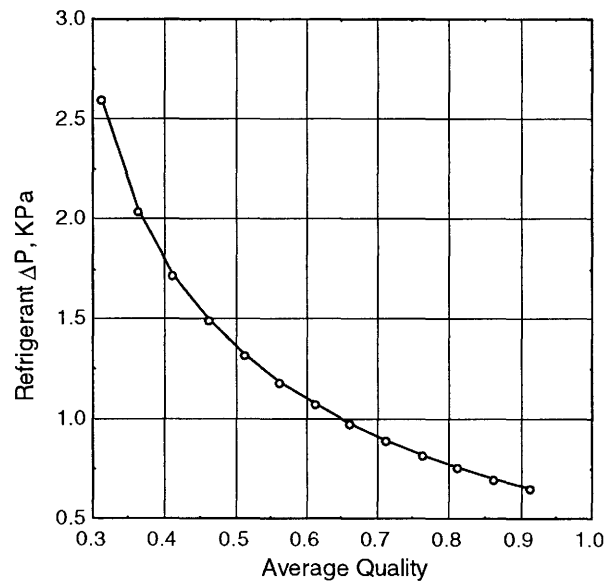


Figure 50. Refrigerant Pressure Drop Per Quality Increment
(Hydronically Coupled Evaporator)

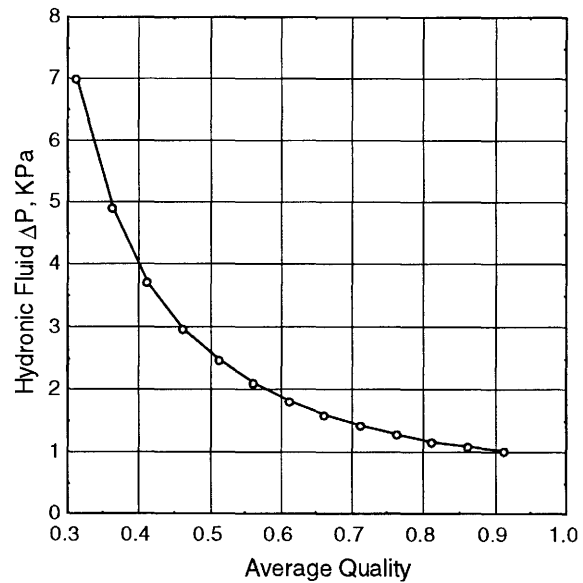


Figure 51. Hydronic Fluid Pressure Drop Per Quality Increment
(Hydronically Coupled Evaporator)

CHAPTER 6. COMPARISON OF THE TWO SYSTEMS

The optimized air-coupled and hydronically coupled microchannel heat pump systems were compared with the results from the round-tube ORNL Heat Pump Design Model (Mark V, Version 95d) (Rice and Jackson, 1994) using system performance and heat exchanger size as evaluation criteria. The optimized geometries and system performances for both the air-coupled and hydronically coupled microchannel heat pumps were listed in Chapter 3. The heat exchanger geometries of the round tube air-coupled system calculated using the ORNL Heat Pump Model are listed in Table 24, and the performance of this system is shown in Table 25. The performance variation of the round-tube heat pump as a function of key parameters was also investigated using the ORNL Heat Pump Design Model.

Figures 52 and 53 show the variation of COP in the cooling mode with changes in indoor unit geometry. It can be seen in Figure 52 that a larger fin density results in a higher COP because of the larger heat transfer area. However, when dehumidification occurs, an extremely small fin pitch may decrease the COP due to holdup of the condensate between the

Table 24. Baseline Configuration of the Round-Tube Heat Pump

	Indoor Unit	Outdoor Unit
Outer tube diameter, m (in)	0.0085 (0.3325)	0.0100 (0.3950)
Inner tube diameter, m (in)	0.0078 (0.3085)	0.0094 (0.3710)
Horizontal tube spacing, m (in)	0.0159 (0.625)	0.0220 (0.866)
Vertical tube spacing, m (in)	0.0254 (1)	0.0254 (1)
Fin pitch, m (1/in)	0.0020 (1/13)	0.0013 (1/20)
Fin thickness, m (in)	0.254e-3 (0.01)	0.127e-3 (0.005)
Fin type	Flat plate	Flat plate
Number of tubes in direction of air flow	4	1
Number of parallel circuits	6	3
Number of return bends	102	21
Heat exchanger frontal area, m ² (ft ²)	0.3532 (3.802)	1.3669 (14.713)

Table 25. Characteristics of the Baseline Round-Tube Heat Pump

	Heating Mode	Cooling Mode
Heat duty (KW)	15.05	10.56
COP	2.459	2.346
Refrigerant charge (kg)	3.807	3.472

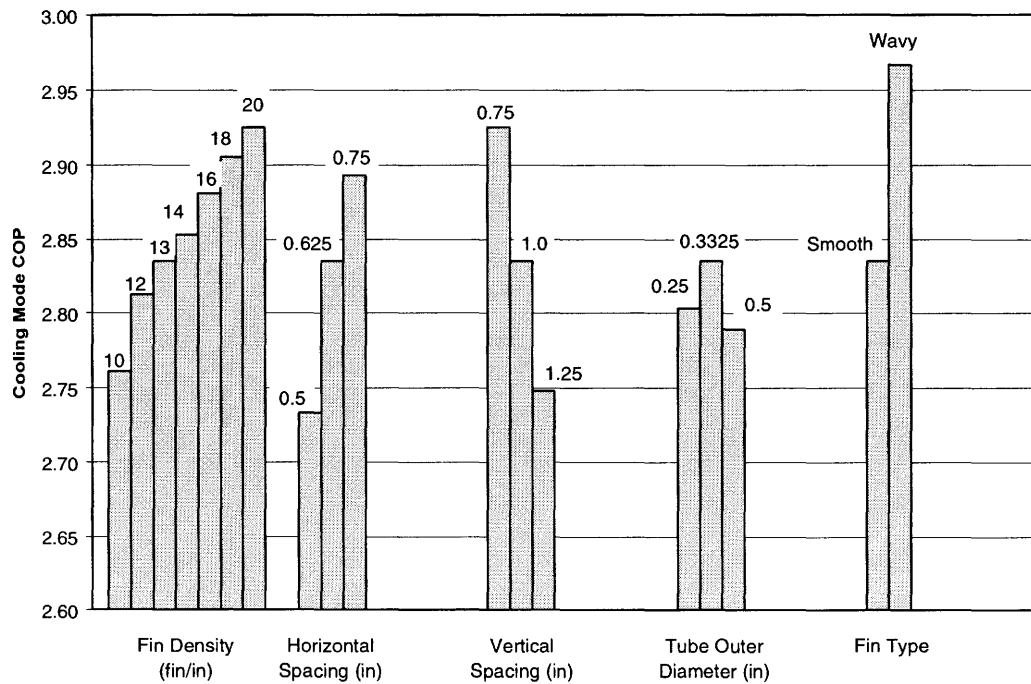


Figure 52. Variation of the Round-Tube Heat Pump Cooling Mode COP with Indoor Unit Tube and Fin Geometry

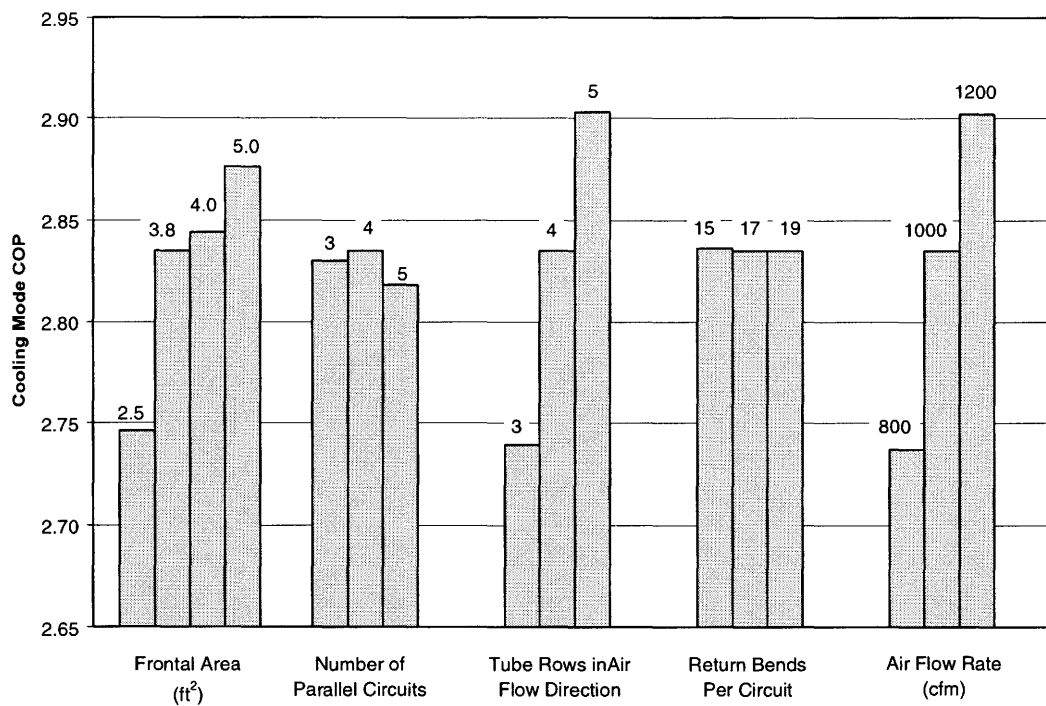


Figure 53 Variation of the Round-Tube Heat Pump Cooling Mode COP with Indoor Unit Design Parameters: Overall Dimensions, Circuiting and Air Flow

fins. Increasing the frontal area or horizontal tube spacing while keeping the total number of tubes constant also increases the COP since this essentially increases the fin surface area. The COP decreases as the vertical tube spacing increases. This is because with the frontal area and tube circuiting unchanged, increasing the vertical tube spacing will decrease the total tube length and thus decrease the tube-side surface area. In addition, the increased spacing decreases the air-side velocity and heat transfer coefficient. The effect of tube diameter on COP is also shown in Figure 52. As the diameter is increased from 0.25 in (0.00635 m) to 0.3325 in (0.00845 m), the COP increases from 2.803 to 2.835. However, a further increase in tube diameter to 0.5 in (0.0127 m) causes a decrease in COP to a value of 2.789. This is because as the tube diameter increases, the refrigerant-side heat transfer coefficient decreases dramatically. For tube outer diameters of 0.25 (0.00635 m), 0.3325 (0.00845 m) and 0.5 in (0.0127 m), the corresponding two-phase heat transfer coefficients are 1112.4 (6317), 651.0 (3697) and 295.9 (1680) Btu/hr·ft²·°F (W/m²·°C), respectively. The increase in the tube surface area does not compensate for this decrease, which results in the decrease in COP as the tube diameter increases from 0.3325 in (0.00845 m) to 0.5 in (0.0127 m). Figure 52 also shows that using wavy fins increase the COP by 5% because of the slight increase in surface area, and the higher air-side heat transfer coefficient. However, this increased performance is at the expense of air-side pressure drop which increased about 29% (0.17 in·H₂O for smooth fin and 0.22 in·H₂O for wavy fin).

Figure 53 shows that for a fixed frontal area, increasing the number of tube rows in the direction of air flow increases both the number of tubes and the fin area, and thus increases the system COP. However, it can be seen that the degree of improvement decreases with increasing tube rows because of the decreasing driving temperature difference available near the air-side exit. The number of tube bends per circuit and the number of parallel circuits do not have a significant effect on the performance of the system, presumably because the tube-side thermal resistance is small compared to the air-side resistance. An increase in air flow rate from 800 to 1200 cfm increases the COP by 6% due to the increase in air-side heat transfer coefficient. However, the pressure drop increases from 0.120 to 0.226 in·H₂O.

Figures 54 and 55 show the variation of the cooling mode COP with changes in the

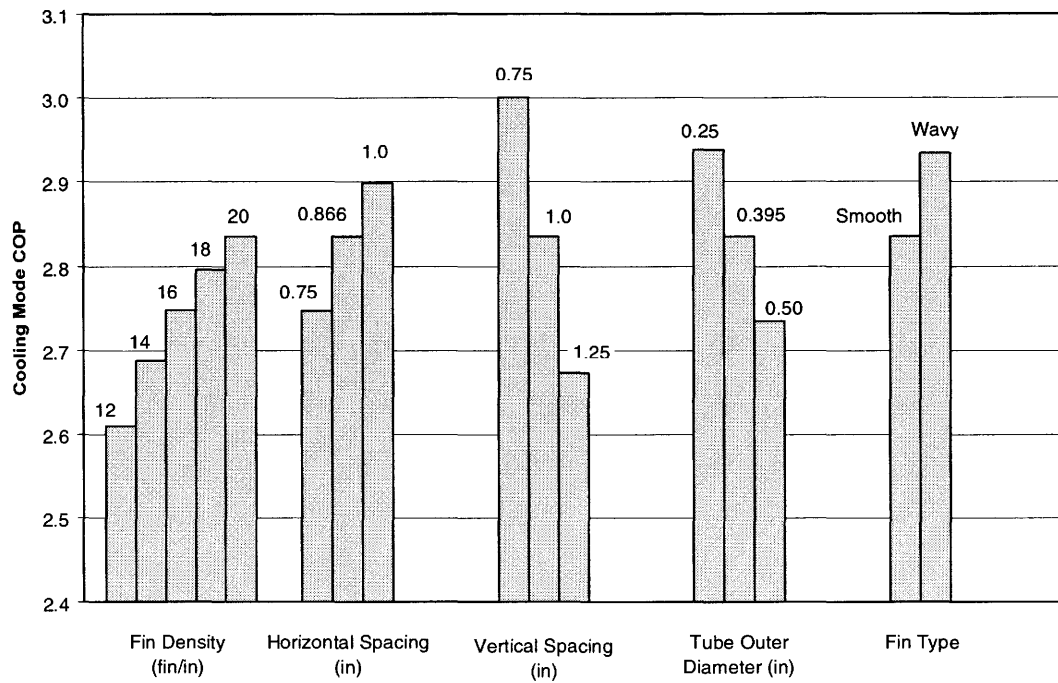


Figure 54. Variation of the Round-Tube Heat Pump Cooling Mode COP with Outdoor Unit Tube and Fin Geometry

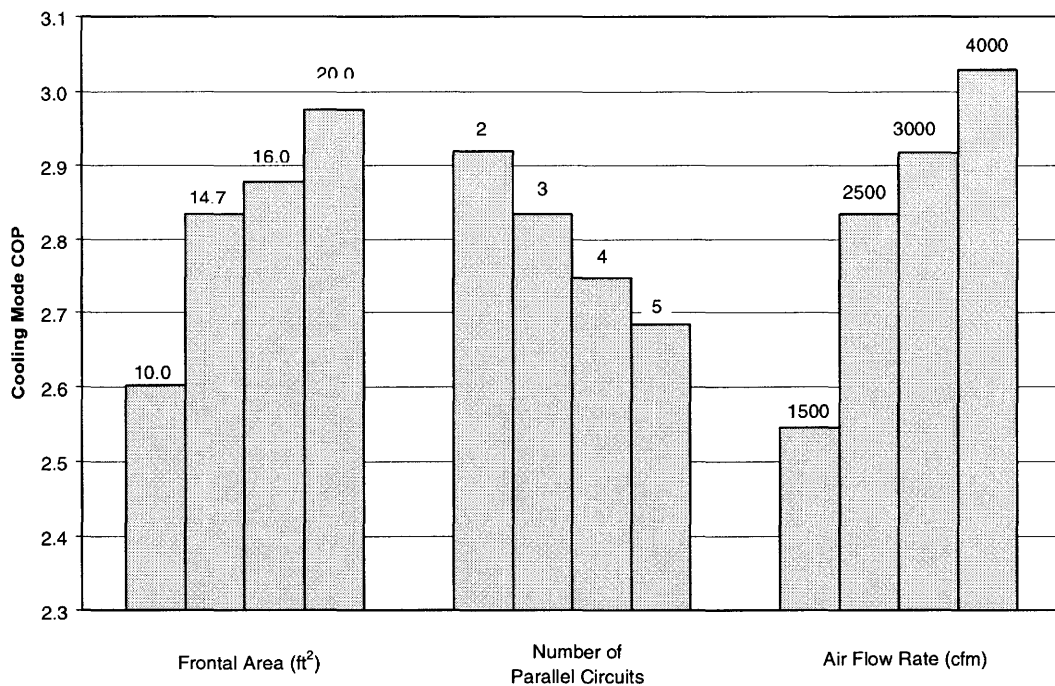


Figure 55. Variation of the Round-Tube Heat Pump Cooling Mode COP with Outdoor Unit Design Parameters: Overall Dimensions, Circuiting and Air Flow

outdoor unit design parameters. As was the case with the indoor unit, a higher fin density results in a higher COP because of the larger heat transfer area. Increasing the frontal area or horizontal tube spacing while keeping the total number of tubes constant also increases the COP since this essentially increases the heat transfer area. With the frontal area and tube circuiting unchanged, increasing the vertical tube spacing would essentially decrease the total tube length and thus decrease the tube side surface area, resulting in a lower COP. As the tube outer diameter increases while other parameters remain unchanged, the COP decreases. This is because large tube diameters would result in large tube-side heat transfer area but a low refrigerant heat transfer coefficient. In addition, the air-side fin surface area decreases. Similar to the indoor unit, using wavy fins increases the COP by 3%. However, the air-side pressure drop increases by about 17% (0.023 in· H₂O smooth fin and 0.027 in· H₂O wavy fin). Figure 55 shows that the COP decreases as the number of parallel circuits increases. Since the frontal area is fixed, increasing the number of parallel circuits decreases the tube length. In addition, more parallel circuits would decrease the refrigerant flow velocity, resulting in a low tube-side heat transfer coefficient. An increase in air flow rate from 1500 to 4000 cfm increases the COP by 19% due to the increase in air-side heat transfer coefficient. However, the pressure drop increases by a factor of almost five (from 0.01 to 0.049 in· H₂O).

The above parametric analysis and discussion validate the choice of the baseline round-tube heat pump configuration. This configuration results in the desired heat duties while keeping the air-side pressure drop within the required range. In the discussion that follows, this configuration is used as the basis for comparison with the air-coupled and hydronically coupled microchannel heat pumps.

It should be noted that the microchannel heat exchangers designed in this study use aluminum as the material of fabrication. However, round tube and fin heat exchangers are typically made of copper and aluminum. Therefore, the mass of round tube and fin heat exchangers can not be directly compared with the mass of microchannel heat exchangers. The material volumes required for the round tube and microchannel heat exchangers, and the heat exchanger face areas were chosen as the criteria for comparison of these different systems.

The material volumes for both round tube and microchannel systems are listed in Table 26. It can be seen that the total material volume of the air-coupled microchannel heat pump is only 36% of the round-tube system. Although the total material volume of the hydronically coupled system is 30% higher than that of the round tube system, the total material volume of the condenser and evaporator, which are the refrigerant carrying heat exchangers, is only 13% of the round tube system. This extremely compact refrigerant loop in the hydronically coupled system allows for significant versatility in packaging and system installation. Furthermore, as will be shown below, the refrigerant charge in this system is extremely low.

The inner volumes of the components and refrigerant lines for these systems are shown in Table 27. The dimensions of refrigerant lines required for these systems are specified in the ORNL Heat Pump Model and are listed in Table 28. It was assumed that the air-coupled microchannel heat pumps also use the same refrigerant lines. It can be seen that a significant

Table 26. Material Volumes of the Heat Exchangers

	Round Tube System	Air-Coupled Microchannel System	Hydronically Coupled Microchannel System
Indoor Unit (m ³)/Ratio	29.44×10 ⁻⁴ / N/A	8.13×10 ⁻⁴ / 27.6%	17.00×10 ⁻⁴ / 57.7%
Outdoor Unit (m ³) /Ratio	30.82×10 ⁻⁴ / N/A	13.77×10 ⁻⁴ / 44.7%	53.24×10 ⁻⁴ / 172.7%
Condenser (m ³) /Ratio	N/A	N/A	3.71×10 ⁻⁴ / 12.6%
Evaporator (m ³) /Ratio	N/A	N/A	4.29×10 ⁻⁴ / 13.9%
Total (m ³) /Ratio	60.26×10 ⁻⁴ / N/A	21.90×10 ⁻⁴ / 36.3%	78.24×10 ⁻⁴ / 129.8%

Note: The "Ratio" is the ratio of Microchannel Heat Exchanger/Round Tube HeatExchanger.

Table 27. Refrigerant Volume

	Round Tube System	Air-Coupled Microchannel System	Hydronically Coupled Microchannel System
Indoor Unit (m ³)	2.68×10 ⁻³	0.91×10 ⁻³	N/A
Outdoor Unit (m ³)	3.75×10 ⁻³	1.13×10 ⁻³	N/A
Condenser (m ³)	N/A	N/A	0.31×10 ⁻³
Evaporator (m ³)	N/A	N/A	0.24×10 ⁻³
Refrigerant Lines	10.15×10 ⁻³	10.15×10 ⁻³	0.35×10 ⁻³
Total (m ³)	16.58×10 ⁻³	12.19×10 ⁻³	0.90×10 ⁻³

amount of the refrigerant needs to be charged in refrigerant lines in air-coupled systems. The mass of the refrigerant was also calculated for both microchannel and round-tube heat pumps. The mass of refrigerant charged in the compressor, heat exchangers and refrigerant lines were estimated based on the average refrigerant density in these components. The refrigerant charges for heating and cooling modes were calculated separately since the function of the indoor and outdoor heat exchangers of the air-coupled systems are different in the heating and cooling modes. The results are shown in Table 29, and once again demonstrate the substantial reduction in charge in the hydronically coupled system.

Figure 56 shows a comparison of the heat exchanger face areas. From this figure, it can be seen that microchannel systems require much smaller face areas compared to round-tube systems, which results in considerable compactness. This figure also shows that the

Table 28. Dimensions of Refrigerant Lines

	Air-Coupled System	Hydronically Coupled System	Length (ft)	Tube Outer Diameter (in)	Tube Wall Thickness (in)
Liquid line to expansion valve	✓		30	0.3125	0.032
Vapor line, reversing valve to indoor coil	✓		30	0.75	0.035
Vapor line, reversing valve to outdoor coil	✓		2	0.75	0.035
Vapor line, reversing valve to compressor inlet	✓		5	0.75	0.035
Vapor line, compressor discharge to reverse valve	✓		2	0.5	0.032
Compressor outlet to condenser	✓		0.5	0.75	0.035
Evaporator to compressor inlet	✓	✓	0.5	0.75	0.035
Condenser outlet to expansion valve	✓	✓	0.5	0.75	0.035

Table 29. Refrigerant Charge

	Heating Mode (kg)	Cooling Mode (kg)
Round Tube System	1.98	1.92
Air-Coupled Microchannel System	1.68	1.52
Hydronically Coupled Microchannel System	0.18	0.20

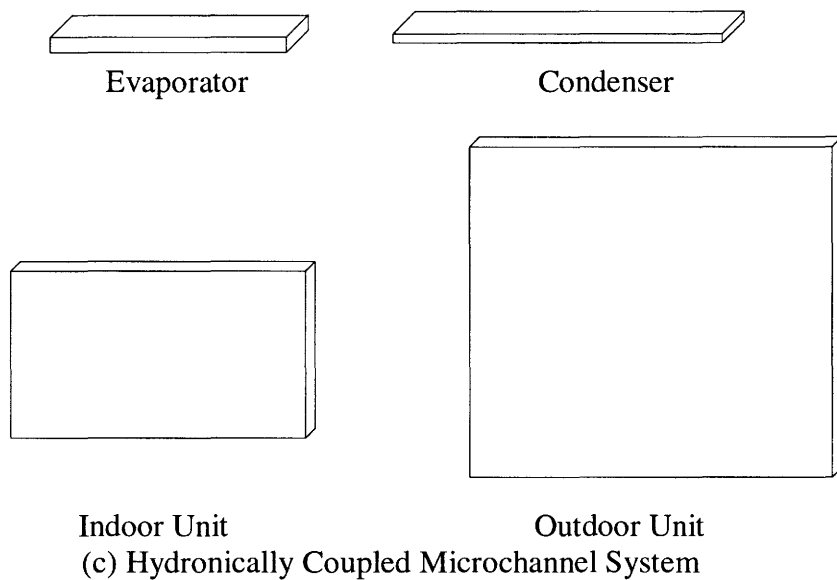
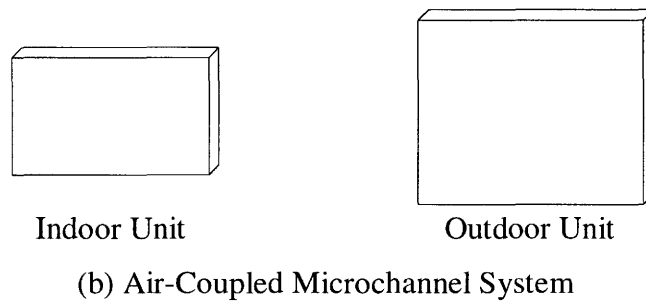
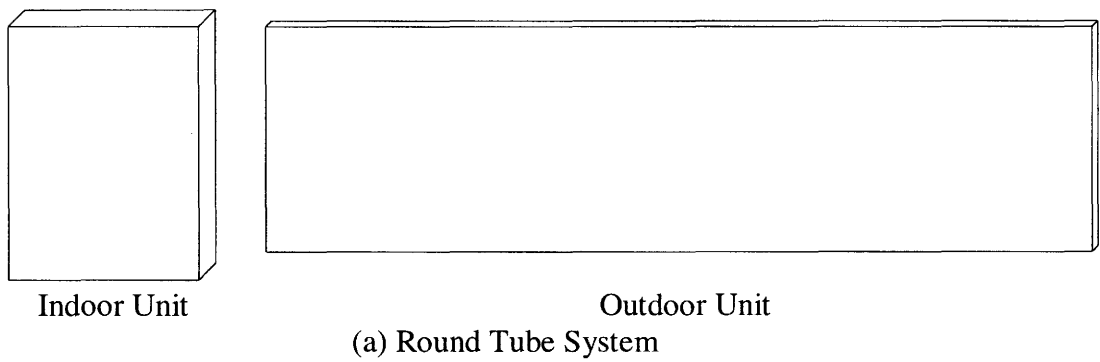


Figure 56. Heat Exchanger Face Area Comparison

hydronically coupled system has an extremely compact condenser and evaporator.

A comparison of the most significant features of these systems is provided in Figure 57. As shown in this figure, to provide same heat duty, the air-coupled microchannel system has the highest COP and the smallest indoor and outdoor heat exchanger frontal areas. In general, microchannel heat pumps also have less refrigerant charge. Especially in hydronically coupled system, with the elimination of refrigerant line, and the significantly compact refrigerant heat exchangers, the refrigerant charge is extremely small.

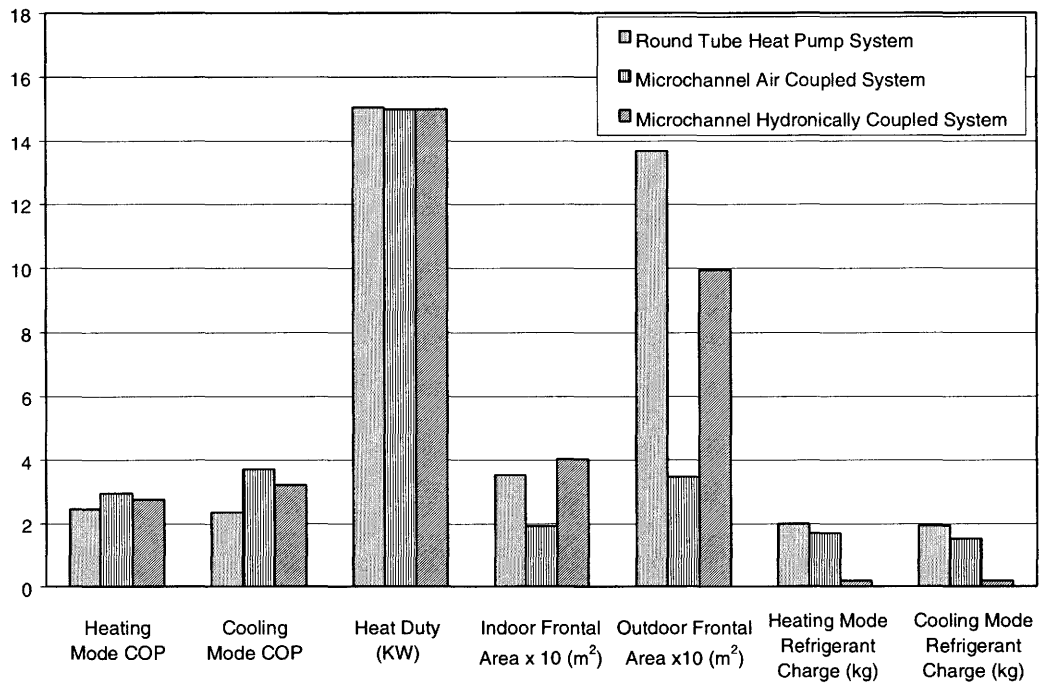


Figure 57. Overall Comparison of the Three Systems

CHAPTER 7. CONCLUSIONS

A detailed investigation of three different types of vapor-compression heat pumps was conducted in this study. Both system level and component level analyses were conducted to design components for these heat pumps that would satisfy the heat transfer requirements within the imposed pressure drop constraints. For the two-phase flow components (evaporators and condensers), the design calculations were conducted on small segments of each heat exchanger so that the variations in heat transfer and pressure drop with vapor quality could be accounted for. The results show that the use of microchannel heat exchangers can provide heating and cooling in a package much smaller than conventional round-tube, flat fin heat exchanger systems. The dimensions of the indoor and outdoor units of the microchannel air-coupled system are $0.57(\text{L}) \times 0.34(\text{H}) \times 0.04(\text{D})$ m and $0.65(\text{L}) \times 0.53(\text{H}) \times 0.045(\text{D})$ m³, respectively. These heat exchangers are only one-half and one-third of the corresponding round tube heat exchangers (indoor unit: $0.52(\text{L}) \times 0.69(\text{H}) \times 0.064(\text{D})$ m, and outdoor unit: $2.24(\text{L}) \times 0.61(\text{H}) \times 0.022(\text{D})$ m). Even further reductions in the refrigerant heat exchangers are possible if the evaporator and condenser are coupled to a hydronic fluid, with both fluids flowing through microchannel geometries. Thus, the hydronically coupled refrigerant heat exchangers have extremely small dimensions, with the condenser being $0.95(\text{L}) \times 0.03(\text{H}) \times 0.09(\text{D})$ m and the evaporator being $0.68(\text{L}) \times 0.04(\text{H}) \times 0.09(\text{D})$ m. Such compact geometries offer significant flexibility in system installation, and the hydronic coupling allows the sealed refrigerant system to be located indoors or outdoors. The hydronically coupled system also offers the potential to be designed as an integrated space-conditioning and water heating system, where the reject heat from the condenser could be used for water heating.

The material needed for microchannel heat pump is also substantially lower than the material requirements for the conventional systems. The total material volume of the air-coupled microchannel heat pump is only 36% of the round tube system, while in the hydronically coupled system, the total material volume of condenser and evaporator is only 13% of the round tube system.

Air-coupled and hydronically coupled systems also result in significant reductions in refrigerant inventories compared to the round tube systems investigated in the present study. The refrigerant charge of the air-coupled system is 20% less than that of the round tube heat pump. For the hydronically coupled system, the refrigerant charge is only 10% of the charge in the round tube heat pump.

The results of this study show that microchannel heat pumps represent not simply an improvement over current technology, but rather a new approach toward the design, fabrication and installation of heating and cooling equipment. The resulting product is compact, modular, thermally efficient, easy to fabricate and install. The drastic reductions in size as well as in material could yield substantial first-cost savings. Finally, the lower refrigerant inventories will minimize CFC and HCFC releases to the atmosphere, thus alleviating the ozone-depletion problem, while potentially higher system efficiencies will mitigate greenhouse gas emissions at the power plant, thus reducing global warming problems.

BIBLIOGRAPHY

- [1] Achaichia, A. and Cowell, T. A., 1988, "Heat Transfer and Pressure Drop Characteristics of Flat Tube and Louvered Plate Fin Surfaces," *Experimental Thermal and Fluid Science*, Vol. 1, pp. 147-157.
- [2] ASHRAE, ASHRAE Handbook—Fundamentals, Chapter 18.
- [3] Bhatti, M. S. and Shah, R. K., 1987, "Turbulent and Transition Flow Convective Heat Transfer in Ducts," in "Handbook of Single-Phase Convective Heat Transfer," eds. Kakac, S., Shah, R. K. and Aung, W., Wiley, pp. 4.1-4-166.
- [4] Butterworth, D., 1975, "A comparison of Some Void-Fraction Relationships for Co-Current Gas-Liquid Flow," *International Journal of Multiphase Flow*, Vol. 1, pp. 845-850.
- [5] Carey, Van P., 1992, "Liquid-Vapor Phase-Change Phenomena: An Introduction to the Thermophysics of Vaporization and Condensation Processes in Heat Transfer Equipment," Hemisphere Publishing Corporation.
- [6] Chaddock, J. B. and Noerager, J. A., 1966, "Evaporation of Refrigerant 12 in a Horizontal Tube with a Constant Wall Heat Flux," *ASHRAE Transactions*, Vol. 72, Part 1.
- [7] Chang, Y. J. and Wang, C. C., 1997, "A Generalized Heat Transfer Correlation for Louver Fin Geometry," *International Journal of Heat and Mass Transfer*, Vol. 40, No. 3, pp. 533-544.
- [8] Chen, S. L., Cheng, Y. R., Liu, C. H. and Jwo, C. S., 2000, "Simulation of Refrigerants Flowing Through Adiabatic Capillary Tubes," *International Journal of Heating, Ventilating, Air-Conditioning and Refrigerating Research*, Vol. 6, No. 2, pp. 101-116.
- [9] Chen, J. C., 1966, "Correlation for Boiling Heat Transfer to Saturated Fluids in Convective Flow," *Ind. Eng. Chem. Proc. Design and Dev.*, Vol. 5, No. 3, pp. 322-339.

- [10] Churchill, S. W., 1977a, "Comprehensive Correlating Equations for Heat Mass and Momentum Transfer in fully Developed Flow in Smooth Tubes," *Ind. Eng. Chem. Fundam.*, Vol. 16, No. 1, pp. 109-116.
- [11] Churchill, S. W., 1977b, "Friction-Factor Equation Spans all Fluid flow Regimes," *Chem. Eng.*, pp. 91-92.
- [12] Cowell, T. A., Heikal, M. R. and Achaichia, A., 1995, "Flow and Heat Transfer in Compact Louvered Fin Surfaces," *Experimental Thermal and Fluid Science*, Vol. 10, pp. 192-199.
- [13] Dittus, F. W. and Boelter, L. M. K., 1930, "Publications on Engineering," University of California, Berkeley, Vol. 2., pp. 443.
- [14] Fischer, S. K., and Rice, C. K., 1983, "The Oak Ridge Heat Pump Models: I. A Steady-State Computer Design Model for Air-to-Air Heat Pumps." Technical Report ORNL/CON-80/R1, Oak Ridge National Laboratory, Oak Ridge, Tenn.
- [15] Fischer, S. K., Rice, C. K. and Jackson, W. L., 1988, "The Oak Ridge Heat Pump Design Models: Mark III Version Program Documentation." ORNL/TM-10192, Oak Ridge National Laboratory, Oak ridge, Tenn.
- [16] Gan, A. I., Klein, S. A. and Reindl, D. T., 2000, "Analysis of Refrigerator/Freezer Appliances Having Dual Refrigeration Cycles," *ASHRAE Transactions*, Vol. 106, Pt. 2.
- [17] Garimella, S., Coleman, J. W. and Wicht, A, 1997, "Tube and Fin Geometry Alternatives for the Design of Absorption-heat-Pump Heat Exchangers," *Enhanced Heat Transfer*, Vol. 4, pp. 217-235.
- [18] Garimella, S. and Wicht, A, 1995, "Air-Cooled Condensation of Ammonia in Flat-Tube, Multi-Louver Fin Heat Exchangers," *Enhanced Heat/Mass Transfer and Energy Efficiency*, ASME, pp. 47-58.
- [19] Groll, E. A., 1997, "Modeling of Absorption/Compression Cycles Using Working Pair Carbon Dioxide/Acetone," *ASHRAE Transactions*, Vol. 103, Pt. 1.
- [20] Hewitt, G. F., Shires, G. L., Bott, T. R., 1993, "Process Heat Transfer," Begell House.

- [21] Jähnig, D. I., Reindl, D. T. and Klein, S. A., 2000, "A Semi-Empirical method for Representing Domestic Refrigerator/Freezer Compressor Calorimeter Test Data," ASHRAE Transactions, Vol. 106, pt. 2.
- [22] Jungnickel, H., Agsten, R., and Kraus, W. E., 1990. Grundlagen der Kältetechnik 2. Berlin: Auflage, Verlag Technik GmbH.
- [23] Kakac, S., Shah, R. K., and Aung, W., 1987, "Handbook of Single-Phase Convective Heat Transfer," Wiley, New York.
- [24] Kuehn, Thomas H., Ramsey, James W., Threlkeld, James L., 1998, "Thermal Environmental Engineering," 3rd ED, Prentice-Hall, pp. 309-326.
- [25] Kyle, D. M., May, 1993, "The Oak Ridge National Laboratory Automobile Heat Pump Model: User's Guide."
- [26] Heat and Mass Transfer Section, Scientific Council, USSR Academy of Sciences, 1976, "Tabular Data for Calculating Burnout When Boiling Water in Uniformly Heated Round Tubes," Thermal Eng. (USSR). English transl., Vol. 23. No. 9, pp. 90-92.
- [27] Levitan, L. L., and Lantsman, F. P., 1975, "Investigating Burnout with Flow of a Steam-Water Mixture in a Round Tube," Thermal Eng. (USSR), English transl., Vol. 22. No. 1, pp. 102-105
- [28] Lockhart, R. W., and Martinelli, R. C., 1949, "Proposed Correlation of Data for Isothermal Two-Phase, Two-Component Flow in Pipes," Chemical Engineering Process, Vol. 45, No. 1, pp. 39-48.
- [29] Purday, H. F. P., 1949, "An Introduction to the Mechanics of Viscous Flow," Dover, New York.
- [30] Rice, C. K., 1991, "The ORNL Modulating Heat Pump Design Tool—User's Guide (Draft)." ORNL/CON-343, Oak Ridge National Laboratory, Oak Ridge, Tenn.
- [31] Rice, C. K. and Jackson, W. L., 1994, "PUREZ—The Mark V ORNL Heat Pump Design Model for Chlorine-Free, Pure and Near-Azeotropic Refrigerant Alternatives (Preliminary Documentation Package)," July 1994, Oak Ridge National Laboratory, Oak Ridge, Tenn.

- [32] Sahnoun, A. and Webb, R. L., November, 1992, "Prediction of Heat Transfer and Friction for the Louver Fin Geometry," *Journal of Heat Transfer*, Vol. 114, pp. 893-900.
- [33] Shah, M. M., 1989, "A General correlation for Heat Transfer During Film Condensation Inside Pipes," *International Journal of Heat and Mass Transfer*, Vol. 22, pp. 547-556.
- [34] Shah, R. K., and Bhatti, M. S., 1987, "Laminar Convective Heat Transfer in Ducts," in "Handbook of Single-Phase Convective Heat Transfer," eds. Kakac, S., Shah, R. K. and Aung, W., Wiley, pp. 3.1-3.137.
- [35] Sunden, B., and Svantesson, J., 1992, "Correlations of j- and f-Factors for Multilouvered Heat Transfer surfaces," *Proceedings of the 3rd UK National Conference Incorporating 1st European Conference on Thermal Sciences*, I. Chem. 92, pp. 805-811.
- [36] Sunden, B., and Svantesson, J., 1992, "Thermal Hydraulic Performance of Some Standard Multilouvered Surfaces," *Heat and Technology*, Vol. 10, No. 3-4, pp. 16-32.
- [37] Sunden, B., and Svantesson, J., 1991, "heat Transfer and Pressure Drop from Louvered Surfaces in Automotive Heat Exchangers," *Experimental heat Transfer*, Vol. 4, pp. 111-125.
- [38] Traviss, D. P., Rohsenow, W. M., and Baron, A. B., 1973, "Forced-Convection Condensation Inside Tubes: A Heat Transfer Equation for Condenser Design," *ASHRAE Transactions*, Vol. 79, Part 1, pp. 157-165.